UNIVERSITY OF CALIFORNIA

Santa Barbara

Modeling and Computation of Immersed, Flexible Boundaries in Complex Fluids

A Dissertation submitted in partial satisfaction
of the requirements for the degree of

Doctor of Philosophy

in

Mathematics

by

Daniel Salazar

Committee in Charge:

Professor Hector D. Ceniceros, Chair

Professor Carlos J. Garcia-Cervera

Professor Paul J. Atzberger

December 2014

The Dissertation of
Daniel Salazar is approved:

_____

Professor Carlos J. Garcia-Cervera

_____

Professor Paul J. Atzberger

_____

Professor Hector D. Ceniceros, Committee Chairperson

October 2014

Modeling and Computation of Immersed, Flexible Boundaries in Complex Fluids

ACKNOWLEDGEMENTS

To Jayne. Thank you for all your support.

VITA OF DANIEL SALAZAR

EDUCATION

Bachelor of Arts in Mathematics, University of California, Santa Barbara, June 2008

Master of Arts in Mathematics, University of California, Santa Barbara, June 2010

Doctor of Philosophy in Mathematics, University of California, Santa Barbara, December 2014 (expected)

PROFESSIONAL EMPLOYMENT

2008-2010: Teaching Assistant, Department of Mathematics, University of California, Santa Barbara

2010-2014: Research Assistant, Department of Mathematics, University of California, Santa Barbara

TECHNICAL SKILLS

Programming Languages and Environments: Fortran, Python, Matlab, Java, LaTeX, Gnuplot, Emacs

FIELDS OF STUDY

Non-Newtonian fluids, microscopic swimming, multiresolution analysis, Immersed Boundary Method

<div align="center">

Abstract

Modeling and Computation of Immersed, Flexible Boundaries in Complex Fluids

Daniel Salazar

</div>

This thesis consists of two main parts related to the modeling and computation of elastic, immersed fiber-like structures in non-Newtonian flows. We focus on the particular case of a flexible, microscopic swimmer which is modeled as an immersed sheet of finite extent in a two-dimensional, incompressible viscoelastic flow at zero Reynolds number. The swimmer is imposed a beating pattern or gait based on a given target curvature. In the first part, we present a comprehensive numerical investigation of such a swimmer in an Oldroyd-B fluid. An efficient semi-implicit version of the Immersed Boundary Method is employed to remove the impeding time-step limitation, induced by the strong interfacial forces needed to appropriately impose the swimmer's gait and inextensibility. Our study investigates in detail, for the first time, the important effects of the domain size, the stiffness parameters enforcing the constraints, and numerical resolution and dissipation. It is found that when the gait is accurately enforced, the mean propulsion speed of the swimmer always decreases monotonically with Deborah number De, which is a measure of the flow's viscoelasticity, i.e. viscoelasticity hinders locomotion. We observe that this monotonic ordering can be broken when the enforcement of the gait is sufficiently relaxed but without viscoelastic swimmer's mean speed

surpassing that of the Newtonian swimmer. More importantly, our investigation reveals that the addition of dissipation in the polymeric stress invariably enhances locomotion and can lead to a speed-up with respect to the Newtonian swimmer. This result clarifies and reconciles several seemingly contradictory existing numerical and experimental results and identifies diffusive transport of momentum via the addition of polymeric stress dissipation as the main mechanism which can produce a swimmer's speed-up in the viscoelastic fluid.

The second part of of this thesis presents a novel multi-scale approach for the computation of the same type of finite swimmer but in a FENE (Finitely Extensible Nonlinear Elastic) fluid. The FENE model overcomes the main limitation of the Oldroyd B fluid which is the possibility of infinite extensions to the polymer chains (modeled as elastic dumbbells) but it requires a full resolution of the dynamics in the polymer's configuration space to evaluate the polymeric stress. When coupled with a flow, this becomes a highly dimensional multi-scale problem which is common to most models of complex fluids arising from kinetic theory and represents a formidable computational challenge. Here, we exploit that the flow affected by the non-inertial swimmer is highly localized and hence an adaptive multi-resolution approach can be effectively implemented. We combine this multi-resolution strategy with a robust, spectral method to solve cost-effectively for the polymer chain dynamics in configuration space. The overall adaptive,

multi-resolution method offers a significant computational improvement over the

direct approach, being about seven faster for this particular application.

Contents

List of Tables

List of Figures

Chapter 1

Introduction

The interaction of flows with immersed, elastic structures is common to a myriad of applications related to biology including, among many others, cardiac flows [23], peristaltic pumping [31, 4], and microscopic swimmers [32, 34, 9, 21]. In this work we focus on the particular case of a microscopic swimmer of finite extent (non-periodic) propelling in a viscoelastic flow by sending lateral waves of motion.

G.I. Taylor provided the first analytic study of small-amplitude, periodic, flexible swimmers in Stokes flow, modeled as infinite (periodic), thin sheets undergoing a sinusoidal wave [30]. He found that, to leading order, the swimmer's propulsion speed is proportional to the square of the wave's amplitude. In this seminal work, Taylor also emphasized that for microscopic swimmers, the propulsion occurs without much displacement of fluid in contrast to (inertial) swimming at

larger length scales. He shows that asymptotically the velocity decays exponentially in the normal direction of the swimmer. Thus, only a localized fluid region around the swimmer is effectively affected.

Often, the flow in which swimming takes place is viscoelastic. Lauga [18, 19] and Fu, Powers and Wolgemuth[12, 11] extended Taylor's asymptotic work to simple Maxwellian models of viscoelastic fluids such as Oldroyd B. They found that for *periodic* swimmers with a prescribed sinusoidal beating pattern at zero Reynolds number, and in the limit of small amplitude, viscoelasticity always hinders locomotion. That is, there is a monotonic decrease of the mean propulsion of the swimmer as the Deborah number De (the ratio of the viscoelastic relaxation time and the characteristic time scale of the swimming motion) increases.

This situation is less clear for a swimmer of finite extent and undergoing a larger amplitude motion. In fact, published experimental and numerical results appear to be contradictory. For example, Liu, Powers and Brewer [21] conducted experiments of a small-amplitude helical swimmer in a Boger fluid and observed that viscoelasticity could enhance its propulsion. Espinosa-Garcia, Lauga, and Zenit [9] performed experiments using swimmers consisting of a flexible tail attached to a magnetically actuated head in a Boger fluid and found that viscoelasticity monotonically increases the ratio of non-Newtonian to Newtonian mean propulsion speed. On the other hand, experiments of Shen and Arratia [27] for *C. elegans nematodes* in shear thinning polymeric fluids, show that viscoelasticity

2

hinders locomotion; the mean propulsion speed decreases with Deborah number, and is always bounded above by Newtonian swimmer's speed. This is to be contrasted with the numerical work of Teran, Fauci, and Shelley [32] who concluded that for a finite swimmer undergoing undulatory motion in an Oldroyd-B fluid, viscoelasticity can not only increase mean propulsion speed (relative to the Newtonian swimmer), but that there exists an optimal Deborah number. There is a recent (under review) numerical work by Thomases and Guy [34] in which an attempt is made to reconcile these seemingly contradictory results. They attribute swimming enhancement to the combined gait asymmetry and swimmer elasticity. In the first part of this thesis, we present a comprehensive numerical study which shows that the actual central mechanism to produce a speed-up relative to the Newtonian swimmer is polymer stress diffusion. Without this diffusive transport, viscoelasticity hinders locomotion, in agreement with the observations of Shen and Arratia [27].

We model the swimmer as an immersed filament in a two-dimensional, incompressible fluid using the Immersed Boundary Method [24, 10]. In the first part of this work, we consider a simple Oldroyd B fluid. The main computational challenges are to enforce the inextensibility constraint and the imposed beating pattern or gait as well as to accurately resolve large, and highly localized viscoelastic stresses. Due to large stresses, huge restoring tangential forces have to be generated to prevent the swimmers from stretching/contracting. These

enormous tangential forces induce a severe stability constraint for explicit time integration of the equations of motion [29, 28] and it becomes necessary to treat the interfacial forces implicitly. This is done efficiently with the numerical methodology introduced in [5, 3]. With this non-stiff approach, we are able to effectively enforce the conditions of inextensibility and to accurately prescribe a swimmer's gait for different Deborah numbers. Our numerical study also includes the investigation of the important effects of domain size, the stiffness parameters associated with the constraints, and numerical resolution. We find that when the gait is accurately enforced, the locomotion speed of the inextensible swimmer *monotonically* decreases with increasing De, in agreement with the analytic results for the small-amplitude, periodic swimmer. Moreover, we observe that for such a swimmer there appears to be a tendency toward a limiting, minimal speed as $De \to \infty$, as predicted by the asymptotic results [18]. When the enforcement of the gait is sufficiently relaxed and the swimmer is allowed to deform in response to the local stresses, our study shows that the propulsion speed monotonicity with De can be broken but without achieving a speed-up relative to the Newtonian swimmer. On the other hand, we find that the addition of some diffusion in the polymeric stress (introduced numerically or by modifying the constitutive equation of the stress as done in the numerical works in [32, 34]) invariably enhances the viscoelastic swimmer's locomotion and can indeed lead to a speed-up relative to the New-

tonian swimmer. Thus, our study reveals that diffusive transport is the leading mechanism to produce a speed-up for this type of swimmers.

The Oldroyd-B viscoelastic model can be viewed as a dilute suspension of polymer chains modeled as elastic, Hookean dumbbells in a Newtonian carrier. The linear (Hookean) intramolecular force of the dumbbells makes it possible to obtain a closed, constitutive equation for the stress contributed by the polymer. The existence of such constitutive law enormously reduces the computational cost as it becomes unnecessary to compute statistical information about the configuration state of the polymer chains to calculate the polymeric stress. For this reason Oldroyd B is a popular and computationally attractive model. It is, however, a model with serious flaws. The main problem of Oldyrod B arises precisely because of its linear intramolecular force as it allows for an infinite stretching of the polymer chain. Linked to this unbounded polymer extensibility is also a shear viscosity which is shear-rate independent, an elongational viscosity that goes to infinity at a finite elongation rate [2] , and, as we will show, unbounded stresses.

By using a nonlinear intramolecular force, the Finitely Extensible, Nonlinearly Elastic (FENE) model [2, 17], overcomes the aforementioned problems of the Oldroyd B model and thus represents a physically more sound model of a dilute polymer solution. However, this comes at a very high computational expense as there is no longer a constitutive equation for the polymeric stress in the FENE model. We need to compute both the configurational dynamics of the polymer

chains to obtain the polymeric stress and the flow. That is, the FENE model couples the configurational and physical spaces rendering a high dimensional problem. Unfortunately this is the norm rather than the exception for kinetic theory models of complex fluids [2, 7, 17], which couple a micro or meso scale structure (e.g. a mechanical model of a polymer chain) with a macro scale flow. The accurate numerical simulation of these multi-scale models is a formidable challenge. The FENE model provides a suitable test bed from which substantial computational advances could be developed for a wider class of kinetic theory models. Attempts have been made to address these challenges and make the FENE model computationally more tractable. In [20] Leonenko and Phillips describe an adaptive grid method to reduce the complexity of solving the Smoluchowski (or Fokker-Planck) equation, which governs the dynamics of the configurational probability density function, for a 1-dimensional FENE model. Chinesta, Ammar, Leygue, and Keunings [6] propose applying a model reduction technique based on a Proper Generalized Decomposition to the Smoluchoski equation, and Ern and Lelievre [8] present a hybrid adaptive method that dynamically switches between a microscopic and macroscopic model in physical space.

In the second part of this work, we propose an adaptive, multiscale methodology based on a combination of multi-resolution and the use of a robust spectral method for the Smoluchowski equation. Our multiresolution approach stems from the schemes first presented by A. Harten in context of hyperbolic conservation laws

[13, 14], and follows the algorithm proposed in [26]. The central idea of our approach is to exploit that viscoelastic stresses are highly localized and thus we can focus our computational efforts in these regions. Moreover, as the Smoluchowski equation has to be solved at each point of the physical space grid, it is crucial to do this with an accurate, cost effective, low memory method; a spectral method meets these requirements. These two ingredients are combined to produce an efficient calculation of the polymer stress by performing a multi-resolution analysis on the spectral coefficients of the configurational probability density function in physical space. Consequently, the spectral method allows to use a reduced number of spectral coefficients or collocation points *in configurational space* while the multi-resolution strategy adaptively focuses the computation of these coefficients *in physical space* to regions of high stresses. We show that this multi-resolution/spectral methodology offers a significant computational improvement over the standard approach, being close to seven times faster for this particular application.

The rest of this thesis is organized as follows: In Chapter 2 we present the mathematical framework for the fluid, swimmer, and viscoelastic models. In Chapter 3 we present the numerical discretizations, and Chapter 4 contains validation studies for them. The main results of our study for an Oldroyd B finite swimmer are found in Chapter 5, and the adaptive multiresolution method is reviewed, tested and analyzed in Chapter 6.

Chapter 2

The Model

We model the swimmer as an inextensible sheet which undergoes imposed lateral waves in a two-dimensional, incompressible, Stokesian flow. The lateral waving motion or gait gives rise to stresses that cause the forward propulsion of the swimmer. This model goes back to a seminal paper of Taylor [30] on the swimming of microscopic organisms. Our work focuses on the particular case in which the sheet is of finite extent (i.e. non-periodic) and the viscoelastic fluid is modeled by a dilute solution of elastic polymer chains with a single relaxation time.

The equations governing the flow can be written as [2, 17]

$$\nabla p = \eta_s \nabla^2 \mathbf{u} + \nabla \cdot \boldsymbol{\tau}_p + \mathbf{F}, \tag{2.1}$$

$$\nabla \cdot \mathbf{u} = 0, \tag{2.2}$$

in a domain Ω, where p is the pressure, η_s is viscosity due to the solvent, $\mathbf{u}$ is the velocity field, $\mathbf{F}$ is the force on the sheet resulting from the imposed gait and the inextensibility constraint, and $\boldsymbol{\tau}_p$ is extra stress due to the polymers, which is given by Kramers formula [2]

$$\boldsymbol{\tau}_p = -n_p k_B T \mathbf{I} + n_p \left\langle \mathbf{Q} \otimes \tilde{\mathbf{F}} \right\rangle_\psi. \tag{2.3}$$

In (2.3), n_p is the density of polymer chains, k_B is the Boltzmann constant, T is the temperature, $\tilde{\mathbf{F}}$ is the intramolecular force, and ψ is probability density function of finding a dumbbell with end-to-end displacement $\mathbf{Q}$. The probability density function, ψ, is computed via [2]

$$\frac{D\psi}{Dt} = -\nabla \cdot \left\{ \left(\nabla \mathbf{u} \cdot \mathbf{Q} - \frac{2}{\zeta} \tilde{\mathbf{F}} \right) \psi \right\} + \frac{2 k_b T}{\zeta} \Delta \psi, \tag{2.4}$$

where ζ is a friction coefficient, $\frac{D\psi}{Dt} = \frac{\partial \psi}{\partial t} + \mathbf{u} \cdot \nabla \psi$, and $\psi = \psi(t, \mathbf{x}, \mathbf{Q})$.

If we introduce the dimensionless quantities in physical space,

$$\boldsymbol{\tau}_p{}' = \frac{L \boldsymbol{\tau}_p}{\eta_0 U}, \qquad x' = \frac{x}{L}, \qquad \boldsymbol{u}' = \frac{\boldsymbol{u}}{U} \tag{2.5}$$

$$t' = \frac{tU}{L}, \qquad p' = \frac{pL}{\eta_0 U}, \qquad \boldsymbol{F}' = \frac{\boldsymbol{F} L^2}{\eta_0 U}, \tag{2.6}$$

and in configuration space,

$$\boldsymbol{Q}' = \frac{\boldsymbol{Q}}{L_q}, \qquad \tilde{\mathbf{F}}' = \frac{\tilde{\mathbf{F}}}{L_q H} \tag{2.7}$$

where U, L, U_q and L_q are characteristic velocity and lengths in physical and configuration space, respectively, then we can rewrite the entire system in dimensionless form as

$$\nabla p = (1 - \epsilon)\nabla^2 \mathbf{u} + \nabla \cdot \boldsymbol{\tau}_p + \mathbf{F}, \tag{2.8}$$

$$\nabla \cdot \mathbf{u} = 0 \tag{2.9}$$

$$\boldsymbol{\tau}_p = \frac{\epsilon}{De}\left(\left\langle \mathbf{Q} \otimes \tilde{\mathbf{F}} \right\rangle_\psi - \mathbf{I} \right) \tag{2.10}$$

$$\frac{D\psi}{Dt} = -\nabla \cdot \left\{ \left(\nabla \mathbf{u} \cdot \mathbf{Q} - \frac{1}{2De}\tilde{\mathbf{F}} \right) \psi \right\} + \frac{1}{2De}\Delta\psi, \tag{2.11}$$

where we have made use of the definitions and rescalings,

$$\lambda_H = \frac{\zeta}{4H}, \qquad De = \frac{\lambda_H U}{L}, \qquad \eta_p = n_p k_B T \lambda_H \tag{2.12}$$

$$\epsilon = \frac{\eta_p}{\eta_0}, \qquad \frac{L_q^2 H}{k_B T} = 1, \qquad \eta_0 = \eta_s + \eta_p, \tag{2.13}$$

and H is a scalar quantity related to the intramolecular force strength.

The swimmer (a sheet) Γ is represented in parametric form as $\mathbf{X}(s,t)$, where s is a Lagrangian variable and t stands for time. We use the IB framework [24] to describe the interaction of the flow and the swimmer. Namely, the interfacial

force $\mathbf{F}$ is written as a delta distribution of a force density $\mathcal{A}(\mathbf{X}(s,t))$ by

$$\mathbf{F}(\mathbf{x},t) = \int_\Gamma \mathcal{A}(\mathbf{X}(s,t))\delta\left(\mathbf{x}-\mathbf{X}(s,t)\right) ds \qquad (2.14)$$

and the kinematic condition expressing the continuity of velocity at the swimmer is also given in terms of a delta distribution:

$$\frac{d\mathbf{X}(s,t)}{dt} = \int_\Omega \mathbf{u}(\mathbf{x},t)\delta\left(\mathbf{x}-\mathbf{X}(s,t)\right) d\mathbf{x}. \qquad (2.15)$$

The wave or gait on the swimming sheet is imposed by prescribing a time-periodic, target curvature $\bar{\kappa}(s,t)$. We follow the approach proposed by Fauci and Peskin [10] to enforce both the waving motion and the inextensibilty condition through a density force given by

$$\mathcal{A}(\mathbf{X}(s,t)) = -\frac{\delta E[\mathbf{X}(s,t)]}{\delta \mathbf{X}} \qquad (2.16)$$

where $E[\mathbf{X}]$ is the elastic energy

$$E[\mathbf{X}] = \frac{S_1}{2}\int_\Gamma \left(\left\|\frac{\partial\mathbf{X}(s,t)}{\partial s}\right\| - 1\right)^2 ds + \frac{S_2}{2}\int_\Gamma (\kappa(s,t)-\bar{\kappa}(s,t))^2 ds. \qquad (2.17)$$

Here κ is the sheet's mean curvature. The parameters S_1 and S_2 are arbitrary but have to be selected large enough to effectively enforce the inextensibilty (first term) and the gait (the target curvature $\bar{\kappa}$) at each time step. The target curvature

11

$\bar{\kappa}$ of the swimmer is specified at all times by

$$\bar{\kappa}(s,t) = \tilde{A}(s)k^2 \sin(ks + \omega t), \quad s \in [0, L], \tag{2.18}$$

where $\tilde{A}$ is related to the maximum amplitude of the swimmer's gait, and L is the swimmer's length.

The polymeric structure will be modelled as dumbells connected by a spring. For an Oldroyd-B fluid the force is Hookean ($\tilde{\mathbf{F}} = \mathbf{Q}$ in dimensionless form) and (2.10) becomes

$$\boldsymbol{\tau}_p = \frac{\epsilon}{De}\left(\langle \mathbf{Q} \otimes \mathbf{Q}\rangle_\psi - \mathbf{I}\right). \tag{2.19}$$

In this case (2.19) and (2.11) can be used to show [2] that the polymeric stress $\boldsymbol{\tau}_p$ satisfies the constitutive equation

$$\boldsymbol{\tau}_p + De\,\boldsymbol{\tau}_p{}^\nabla = \epsilon \left[\nabla \mathbf{u} + \nabla \mathbf{u}^T\right], \tag{2.20}$$

where

$$\boldsymbol{\tau}_p{}^\nabla = \frac{\partial \boldsymbol{\tau}_p}{\partial t} + \mathbf{u} \cdot \nabla \boldsymbol{\tau}_p - \left(\nabla \mathbf{u}\,\boldsymbol{\tau}_p + \boldsymbol{\tau}_p \nabla \mathbf{u}^T\right) \tag{2.21}$$

is the upper convective derivative of $\boldsymbol{\tau}_p$ (with the last two terms understood as matrix products). This eliminates the need to solve directly for the the probability distribution function, ψ.

The Finitely Extensible, Nonlinearly Elastic (FENE) model is defined by the nonlinear force $\tilde{\mathbf{F}}(\mathbf{Q}) = \frac{\mathbf{Q}}{1-\mathbf{Q}^2/b}$, where b is a parameter related to the maximal extensibility of the polymer dumbbells. In this case there does not exist a related constitutive equation for the stress and ψ must be found throughout physical space using (2.11). However, as it is shown in Chapter 6, Figure 6.2, under certain flows Oldroyd-B (Hookean) dumbbells can be stretched to unnatural lengths resulting in unbounded stresses. The nonlinear FENE force prevents such behavior.

Chapter 3

Numerical Methods

The physical computational domain is the square $\Omega = [0, C] \times [0, C]$, which is discretized with a uniform Cartesian grid $\mathcal{G}_h$ with $N \times N$ computational cells of size $h \times h$, where $h = C/N$. Periodic boundary conditions are assumed for the flow variables and $\boldsymbol{\tau}_p$. The swimmer Γ is of extent L and is discretized with a uniform grid $\mathcal{G}_{\Delta s}$ in s, consisting of the points $s_i = i\Delta s$, $i = 0, \ldots, N_b$ with $\Delta s = L/N_b$.

Let $\mathbf{D}_h$ and L_h be the standard centered second-order finite difference operators to approximate the gradient and Laplacian, respectively. Given the excess polymeric stress $\boldsymbol{\tau}_p^n$ at the current time t_n, we discretize the Stokes equations and the swimmer's evolution equation as

$$\mathbf{D}_h p^{n+1} - (1 - \epsilon) L_h \mathbf{u}^{n+1} = \mathbf{D}_h \cdot \boldsymbol{\tau}_p{}^n + \mathcal{S}_n \mathcal{A}_{\Delta s}(\mathbf{X}^{n+1}), \qquad (3.1)$$

$$\mathbf{D}_h \cdot \mathbf{u}^{n+1} = 0, \qquad (3.2)$$

$$\frac{\mathbf{X}^{n+1} - \mathbf{X}^n}{\Delta t} = \mathcal{S}_n^* \mathbf{u}^{n+1}, \tag{3.3}$$

where $\mathcal{S}_n$ and $\mathcal{S}_n^*$ are the IB Method spreading and interpolation operators given

by

$$(\mathcal{S}_n \mathbf{g})(\mathbf{x}) = \sum_{s_i \in \mathcal{G}_b} \mathbf{g}(s_i) \delta_h(\mathbf{x} - \mathbf{X}^n(s_i)) \Delta s, \tag{3.4}$$

$$(\mathcal{S}_n^* \mathbf{w})(s) = \sum_{\mathbf{x}_{ij} \in \mathcal{G}} \mathbf{w}(\mathbf{x}_{ij}) \delta_h(\mathbf{x}_{ij} - \mathbf{X}^n(s)) h^2 \tag{3.5}$$

and δ_h is an approximation to the 2D delta distribution, $\delta_h(\mathbf{x}) = \varphi(x) \varphi(y)$,

where $\mathbf{x} = (x, y)$ and [24]

$$\varphi(r) = \begin{cases} \frac{1}{4h} \left(1 + \cos\left(\frac{\pi r}{2h}\right) \right), & \mid r \mid \leq 2h, \\ 0, & \mid r \mid > 2h. \end{cases} \tag{3.6}$$

To compute the force density $\mathcal{A}_{\Delta s}(\mathbf{X})$ we employ the following discretization

of the energy:

$$E_{\Delta s}[\mathbf{X}] = \frac{S_1}{2} \sum_{k=0}^{n} (\|D_{\Delta s} \mathbf{X}_k\| - 1)^2 \Delta s + \frac{S_2}{2} \sum_{k=1}^{n-1} (\kappa_k - \bar{\kappa}_k)^2 \Delta s, \tag{3.7}$$

where $D_{\Delta s}$ stands for the centered finite difference for $k = 1 \ldots n - 1$ and for the

forward and backward finite differences for $k = 0$ and $k = n$, respectively. The

mean curvature κ is computed from $\mathbf{X}(s, t)$ using second order finite differences

and assuming that the target curvature is satisfied exactly at the end points. Then

$$\mathcal{A}_{\Delta s}(\mathbf{X})_j = -\left[\frac{\partial E_{\Delta s}}{\partial X_j}, \frac{\partial E_{\Delta s}}{\partial Y_j}\right]. \tag{3.8}$$

We note that for this discretization the sum of all the forces is zero, i.e. $\sum_k \mathcal{A}_{\Delta s}(\mathbf{X})_k = 0$, which is a compatibility condition for Stokes equations.

Equations (3.1)-(3.3) are an implicit system for the future velocity and sheet configuration, $\mathbf{u}^{n+1}$ and $\mathbf{X}^{n+1}$. To solve this system we follow the approach proposed in [[5],[3]] which we briefly outline next.

The solution to the discrete Stokes equations (3.1)-(3.2) can be written as

$$\mathbf{u}^{n+1} = \mathcal{L}_h\left[\mathcal{S}_n \mathcal{A}_{\Delta s}(\mathbf{X}^{n+1}) + \mathbf{D}_h \cdot \tau_p^n\right], \tag{3.9}$$

where $\mathcal{L}_h$ is the *fluid solver* operator whose application gives the velocity field given the interfacial configuration (and hence the force density) and the excess polymeric stress. We compute $\mathcal{L}_h$ using the Fast Fourier Transform (FFT). Substituting this into (3.3) we obtain an equation for $\mathbf{X}^{n+1}$ only:

$$\mathbf{X}^{n+1} = \mathcal{M}_n \mathcal{A}_{\Delta s}(\mathbf{X}^{n+1}) + \mathbf{b}^n, \tag{3.10}$$

where $\mathcal{M}_n$, the *flow-structure* operator, is given by $\mathcal{M}_n = \Delta t \mathcal{S}_n^* \mathcal{L}_h \mathcal{S}_n$ and

$$\mathbf{b}^n = \mathbf{X}^n + \Delta t \, \mathcal{S}_n^* \mathcal{L}_h \left(\mathbf{D}_h \cdot \tau_p^n \right). \tag{3.11}$$

The relation (3.10) is a nonlinear system for $\mathbf{X}_j^{n+1}$, $j = 0, \ldots, N_b$. It is solved efficiently with Newton's method combined with an expedited evaluation of matrix representation of $\mathcal{M}_n$ as detailed in [5]. Once $\mathbf{X^{n+1}}$ is computed, $\mathbf{u}^{n+1}$ is obtained from (3.9) and the excess stress is updated.

3.1   Obtaining the Stress - Oldroyd-B

For an Oldroyd-B fluid, the governing equations are

$$\nabla p = (1 - \epsilon)\nabla^2 \mathbf{u} + \nabla \cdot \boldsymbol{\tau}_p + \mathbf{F} \tag{3.12}$$

$$\nabla \cdot \mathbf{u} = 0 \tag{3.13}$$

$$\boldsymbol{\tau}_p + De \, \boldsymbol{\tau}_p{}^{\nabla} = \epsilon \left[\nabla \mathbf{u} + \nabla \mathbf{u}^T \right]. \tag{3.14}$$

We define

$$\mathbf{G}(\mathbf{u}, \boldsymbol{\tau}_p) = -\mathbf{u} \cdot \nabla \boldsymbol{\tau}_p + \left(\nabla \mathbf{u} \, \boldsymbol{\tau}_p + \boldsymbol{\tau}_p \, \nabla \mathbf{u}^T \right) + \frac{1}{De} \left(\epsilon \left[\nabla \mathbf{u} + \nabla \mathbf{u}^T \right] - \boldsymbol{\tau}_p \right) \tag{3.15}$$

so that the Oldroyd-B constitutive equation can be expressed by

$$\frac{\partial \boldsymbol{\tau}_p}{\partial t} = \mathbf{G}(\mathbf{u}, \boldsymbol{\tau}_p).\tag{3.16}$$

Let $\mathbf{G}_h$ be the discrete version of (3.15) obtained by using standard second order spatial finite differences for all the terms except for the advection $\mathbf{u} \cdot \nabla \tau_p$ which is computed with a upwind scheme (first-order and third-order as explained later). Then the update equation for the stress is

$$\boldsymbol{\tau}_p^{n+1} = \boldsymbol{\tau}_p^n + \Delta t \mathbf{G}_h(\mathbf{u}^{n+1}, \boldsymbol{\tau}_p^n).\tag{3.17}$$

3.2   Obtaining the Stress - FENE

For the FENE model (2.11) must be solved to obtain ψ. Once ψ is obtained, (2.10) can be used to compute $\boldsymbol{\tau}_p^n$. To discretize (2.11),

$$\frac{D\psi}{Dt} = -\nabla \cdot \left\{ \left(\nabla \mathbf{u} \cdot \mathbf{Q} - \frac{1}{2De}\tilde{\mathbf{F}} \right) \psi \right\} + \frac{1}{2De}\Delta\psi,$$

we follow the approach of Lozinski and Chauvire [22]. Since $|\mathbf{Q}| \in (0, \sqrt{b})$, it is natural to represent the equation in polar coordinates. As such we rewrite (2.11)

18

as

$$\frac{D\psi}{Dt} = -(\kappa_{11} + \kappa_{22})\psi - rb_1\frac{d\psi}{dr} - b_2\frac{d\psi}{d\theta} + \frac{1}{De}\frac{b^2}{(b-r^2)^2}\psi$$
$$+ \frac{1}{2De}\left\{\frac{br}{b-r^2} + \frac{1}{r}\right\} \cdot \frac{d\psi}{dr} + \frac{1}{2De}\left\{\frac{d^2\psi}{dr^2} + \frac{1}{r^2}\frac{d^2\psi}{d\theta^2}\right\}, \qquad (3.18)$$

for $r \in [0, \sqrt{b})$ and $\theta \in [0, 2\pi)$, where

$$b_1 = \frac{\kappa_{11} + \kappa_{22}}{2} + \frac{\kappa_{12} + \kappa_{21}}{2}\sin(2\theta) + \frac{\kappa_{11} - \kappa_{22}}{2}\cos(2\theta) \qquad (3.19)$$

$$b_2 = \frac{\kappa_{21} - \kappa_{12}}{2} + \frac{\kappa_{12} + \kappa_{21}}{2}\cos(2\theta) + \frac{\kappa_{22} - \kappa_{11}}{2}\sin(2\theta). \qquad (3.20)$$

To help prevent the spring force from becoming infinite near $r = \sqrt{b}$, we introduce a new function α that satisfies

$$\psi(t, \boldsymbol{x}, r, \theta) = \left(1 - \frac{r^2}{b}\right)^2 \alpha(t, \boldsymbol{x}, r, \theta), \qquad (3.21)$$

where the prefactor $\left(1 - \frac{r^2}{b}\right)^2$ is chosen such that the boundary conditions,

$$\psi(t, \boldsymbol{x}, \sqrt{b}, \theta) = 0 \qquad (3.22)$$

$$\frac{d\psi}{dr}(t, \boldsymbol{x}, 0, \theta) = 0, \qquad (3.23)$$

are satisfied.

19

To accomodate the spectral discretization, we introduce the change of variables $r^2 = b(1 + \eta)/2$, for $\eta \in (-1, 1)$. In terms of η,

$$\psi(t, \boldsymbol{x}, \eta, \theta) = \left(\frac{1 - \eta}{2}\right)^2 \alpha(t, \boldsymbol{x}, \eta, \theta), \tag{3.24}$$

and the evolution equation for α is written as

$$\frac{D\alpha}{Dt} = -(\kappa_{11} + \kappa_{22})\alpha + b_1 L_1 \alpha - b_2 \frac{d\alpha}{d\theta} + L_0 \alpha, \tag{3.25}$$

where

$$L_0 \alpha = -\frac{4(b - 4)\eta}{bDe(1 - \eta)^2}\alpha + \left(\frac{2(b - 8)(1 + \eta)}{bDe(1 - \eta)} + \frac{4}{bDe}\right)\frac{d\alpha}{d\eta}$$

$$+ \frac{4(1 + \eta)}{bDe}\frac{d^2\alpha}{d\eta^2} + \frac{1}{bDe(1 + \eta)}\frac{d^2\alpha}{d\theta^2} \tag{3.26}$$

$$L_1 \alpha = 4\frac{1 + \eta}{1 - \eta}\alpha - 2(1 + \eta)\frac{d\alpha}{d\eta}. \tag{3.27}$$

Equations (3.25)-(3.27) are discretized using a spectral method, specifically Fourier in θ and Gauss-Legendre collocation in η. As such, any sufficiently regular function $f(\eta, \theta)$ can be represented as

$$f(\eta, \theta) \approx \sum_{i=0}^{1} \sum_{l=i}^{N_f} \sum_{k=1}^{N_r} a_{kl}^i h_k(\eta) \Phi_{il}(\theta) \tag{3.28}$$

with

$$\Phi_{il}(\theta) = (1 - i)\cos(2l\theta) + i\sin(2l\theta), \tag{3.29}$$

and $h_k(\eta)$ the Lagrange interpolating polynomials based on the Gauss-Legendre collocation points η_r. Algorithms for their computation can be found in [16] (Algorithms 22,23). We note that integration in η can be computed using the Gauss quadtrature rule

$$\int_{-1}^{1} f(x)\,dx \approx \sum_{i=1}^{N_r} \omega_i f(x_i), \tag{3.30}$$

with the approximation being exact for polynomials of degree $2(N_r - 1) + 1$ or less.

The spectral basis functions, $\{h_k\}_{k=1}^{N_r}$ and $\{\Phi_{il}\}_{i=0,1,l=0}^{N_f}$, are orthogonal and we define the coefficients for an arbitrary function f as

$$a_{mn}^{j} = \frac{1}{\omega_m(1 + \delta_{n0})\pi} \int_{0}^{2\pi} \int_{-1}^{1} f(\eta, \theta) h_m(\eta) \Phi_{jn}(\theta)\,d\eta\,d\theta \tag{3.31}$$

$$= \frac{1}{(1 + \delta_{n0})\pi} \int_{0}^{2\pi} f(\eta_m, \theta) \Phi_{jn}(\theta)\,d\theta, \tag{3.32}$$

where this last integral can be computed by quadrature, if not analytically.

21

We discretize in time using a first order time-splitting method to decouple the computations in configuration space from those in physical space:

$$\frac{\alpha^* - \alpha^n}{\Delta t} = -(\kappa_{11} + \kappa_{22})\alpha^n + b_1 L_1 \alpha^n - b_2 \frac{d\alpha}{d\theta}^n + L_0 \alpha^* \qquad (3.33)$$

$$\frac{\alpha^{n+1} - \alpha^*}{\Delta t} = -\mathbf{u}^n \cdot \nabla \alpha^* \qquad (3.34)$$

Focusing on the configuration space equation, we let M_0, M_1 and M_2 be the matrix representation of the discretized operators L_0, $b_1 L_1$ and $-b_2 \frac{d\alpha}{d\theta}$, respectfully. Then,

$$\alpha^* = (I - \Delta t M_0)^{-1} \left[(1 - \Delta t(\kappa_{11} + \kappa_{22}))I\alpha^n + \Delta t M_1 \alpha^n + \Delta t M_2 \alpha^n\right]. \qquad (3.35)$$

Once α^* is obtained, (3.34) can be used to compute α^{n+1} and the stress is updated via (3.24), (3.21) and (2.10).

22

Chapter 4

Model Validation

4.1 Newtonian and Oldroyd-B Model Validation

We begin with two validation tests using analytic results for an infinite, periodic sheet in Stokesian flow (zero Reynolds number) undergoing small-amplitude motion.

The sheet is of the form:

$$y(x,t) = a \sin(kx + \omega t). \tag{4.1}$$

Taylor [30] predicted that the sheet's mean locomotion speed for small-amplitude waves $(ak << 1)$ would be

$$U(a,k,\omega) = \frac{1}{2} \left(\frac{\omega}{k} \right) (ak)^2 \left[1 - \frac{19}{16}(ak)^2 \right] + O(ak)^6. \tag{4.2}$$

Moreover, if looked from the frame of reference moving with the sheet, material points would describe figure-eight like paths. For a given small amplitude (up to 5 % of the wavelength), we perform simulations for various resolutions up to the time equal to five wave periods. All the parameters used for this test are provided in Table 4.1.

Ω	$[0,1] \times [0,1]$
Δs	$0.5\Delta x$
Δt	Δs
S_1	10^6
S_2	10^4
k	2π
ω	2π
a	.001, .003, .006, .01,.02, .03, .04, .05

Table 4.1: Parameters for the infinite sheet simulations.

As it is evident in Figure 4.1 there is a convergence to the asymptotic value of Taylor, and the figure-eight path is also confirmed in Figure 4.2.
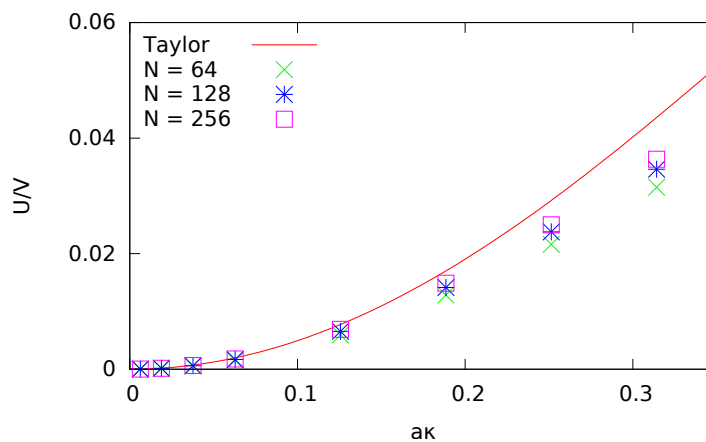
Figure 4.1: Taylor's predicted swim speed and the computed swim speed for $N = 64, 128, 256$.

24
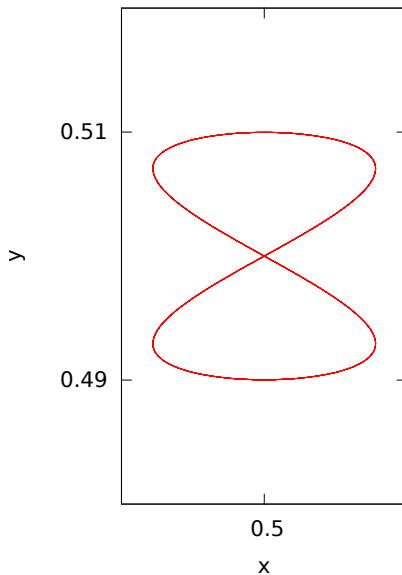
Figure 4.2: Midpoint of the swimmer (amplitude .01) in the frame of reference of the moving sheet. The figure-eight is traversed five times, once for each period.

Our second validation test considers the asymptotic, small amplitude, results of Lauga [18], which state that the ratio of an Oldroyd-B swimmer's mean locomotion speed U_V to a Newtonian swimmer's mean locomotion speed U satisfies

$$\frac{U_V}{U} = \frac{1 + (1 - \epsilon)De^2}{1 + De^2} + O(ak)^2. \tag{4.3}$$

Figure 4.3 shows good agreement between our results and Lauga's prediction for $De = 1$. The parameters for this test are as in Table 4.1 with $\epsilon = 1/3$.

25
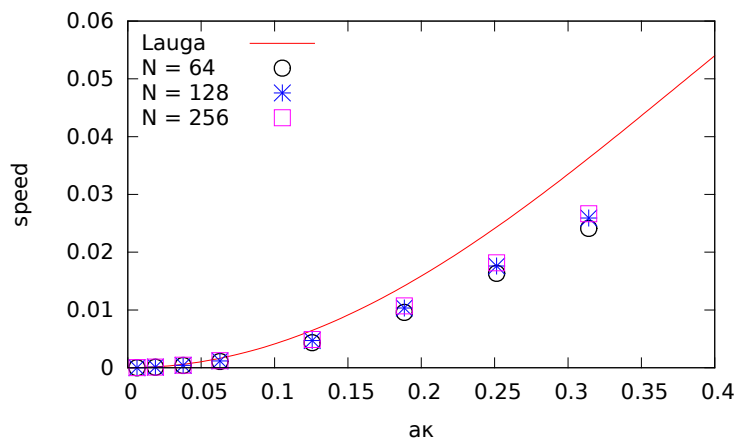
Figure 4.3: Lauga's predicted swim speed and the computed swim speed for $N = 64, 128, 256$ and $De = 1$.

4.2 FENE Model Validation

For this validation test we consider planar extensional flow of the form $\mathbf{u} = c \cdot (x, -y)$, with the velocity gradient, $\nabla \mathbf{u}_{i,j} = \frac{\partial \mathbf{u}_i}{\partial x_j}$, given by

$$\nabla \mathbf{u} = \begin{pmatrix} c & 0 \\ 0 & -c \end{pmatrix}. \tag{4.4}$$

For this case the exact steady state solution is known [2] and, in terms of (η, θ), given by

$$\alpha_{eq}^{\infty} = \left(\frac{1-\eta}{2} \right)^{b/2-2} \exp \left\{ \frac{De \cdot c \cdot b}{2} (1+\eta) (\cos 2\theta) \right\}. \tag{4.5}$$

26

We take

$$\alpha_{eq}^0 = \frac{b+2}{2\pi b}\left(\frac{1-\eta}{2}\right)^{b/2-2} \tag{4.6}$$

as the initial condition, fix the flow rate for all the tests ($c = 1$), and vary De and the extensibility parameter b.

We begin by setting $De = .1$ and consider $b = 10$ and $b = 100$. Figure 4.4 and Figure 4.5 demonstrates the convergence in the L_∞ norm of the difference between the exact and computed solution as a function of time (for $b = 10$ and $b = 100$). Note the larger spectral element requirements for the $b = 100$ case.

Figure 4.4: $\|\alpha_{eq}^\infty - \alpha^n\|_\infty$ with maximal extensibility set to $\sqrt{10}$ and $N_f = 10$, $N_r = 15$, $\Delta t = .01$, and $De = 0.1$.

Figure 4.5: $\|\alpha_{eq}^\infty - \alpha^n\|_\infty$ with maximal extensibility set to $\sqrt{100}$, $\Delta t = .01$, and $De = 0.1$. Note the need for increased spectral resolution due to the greater allowed extensibility and resulting larger domain.

Next we set $De = .5$ and once again consider $b = 10$ and $b = 100$. Figure 4.6 and Figure 4.7 show convergence as a function of time for this larger De. We emphasize that for this particular case, the Oldroyd-B model leads to finite time blow up in the stress (see Figure 6.2), underscoring the need to develop efficient methods for the FENE model.
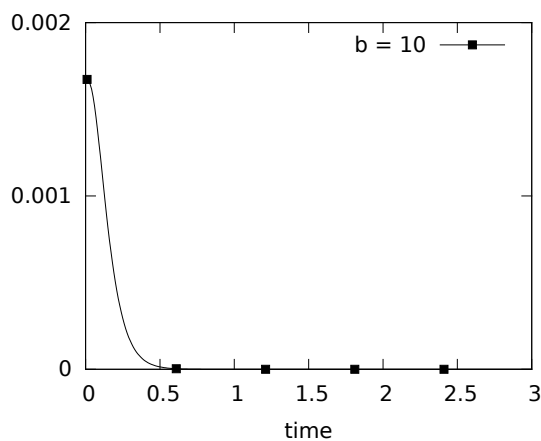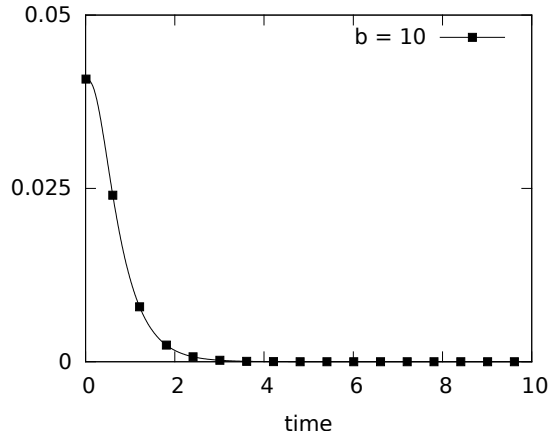
Figure 4.6: $\|\alpha_{eq}^\infty - \alpha^n\|_\infty$ with maximal extensibility set to $\sqrt{10}$ and $N_f = 10$, $N_r = 15$, $\Delta t = .01$, and $De = 0.5$.
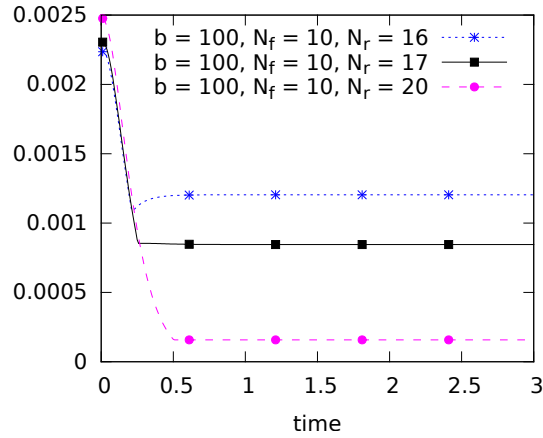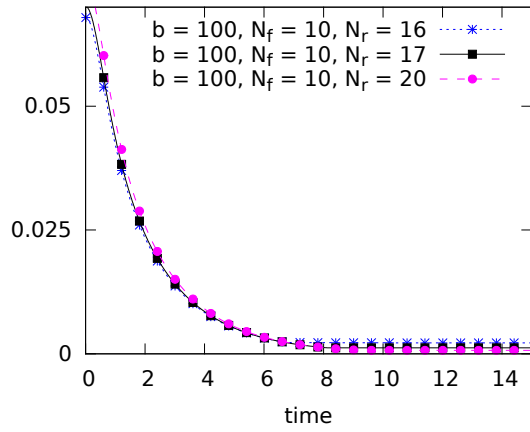

Figure 4.7: $\|\alpha_{eq}^\infty - \alpha^n\|_\infty$ with maximal extensibility set to $\sqrt{100}$, $\Delta t = .01$, and $De = 0.5$. Note the need for increased spectral resolution due to the greater allowed extensibility and resulting larger domain.

Chapter 5

Finite Swimmers in an Oldroyd-B

Fluid

We now focus on the central case of study of this work: a finite swimmer in an Oldroyd-B Stokesian fluid ($Re = 0$). We will consider two distinct swimming motions: kicking and burrowing. For the kicker the undulations increase in amplitude from head to tail, and the target curvature, $\bar{\kappa}$, is specified at all times by

$$\bar{\kappa}(s,t) = -A(s-1)k^2 \sin(ks + \omega t), \quad s \in [0, L], \tag{5.1}$$

where A is the maximum amplitude of the swimmer's gait and L is the swimmer's length. For the burrower the undulations decrease in amplitude from head to tail

and the target curvature is specified by

$$\bar{\kappa}_B(s, t) = A(s + .4)k^2 \sin(ks + \omega t), \quad s \in [0, L]. \tag{5.2}$$

To obtain the swimmer's initial configuration $(x_0(s), y_0(s))$ we integrate the following system:

$$\frac{\partial \theta_0}{\partial s}(s) = \bar{\kappa}(s, 0), \tag{5.3}$$

$$\frac{\partial x_0}{\partial s}(s) = \cos(\theta_0(s)), \tag{5.4}$$

$$\frac{\partial y_0}{\partial s}(s) = \sin(\theta_0(s)). \tag{5.5}$$

To do this, we first integrate analytically (5.3) to get the tangent angle θ_0 (we set the constant of integration to zero). We then integrate the system

$$x_0(s_i) = \int_0^{s_i} \cos(\theta_0(t))dt, \tag{5.6}$$

$$y_0(s_i) = \int_0^{s_i} \sin(\theta_0(t))dt, \tag{5.7}$$

using trapezoid rule for $i = 0, \ldots, N_s$. Here $N_s = [L/\Delta s]$, and $s_i = i\Delta s$.

$N \times N$	Domain
128×128	$[0, 2] \times [0, 2]$
256×256	$[0, 4] \times [0, 4]$
512×512	$[0, 8] \times [0, 8]$

Table 5.1: Computational domains and their discretization.

Δs	$0.5\Delta x$
Δt	$0.5\Delta s$
S_1	10^7
S_2	10^4
L	0.6
k	$\frac{2\pi}{L}$
ω	2π
Final Time	20
A	0.1
ϵ	$\frac{1}{3}$

Table 5.2: Simulation parameters for a finite swimmer in Stokes ($Re = 0$) Oldroyd-B flow.

Given that this is a finite swimmer and we employ periodic boundary conditions, we first look at the effect of the domain size. To this end, we fix the amplitude ($A = 0.1$) and length ($L = 0.6$) of the swimmer. The numerical resolution is kept fixed (by adjusting N and N_b) as we consider different domain sizes (see Table 5.1). We fix $De = 0$ for this test and the remaining numerical parameters are all listed in Table 5.2.

Figure 5.1: Effect of finite domain size on Newtonian ($De = 0$) kicker for domain sizes listed in Table 5.1. (a) location of center of mass throughout 20 periods, (b) location of center of mass during final 2 periods, (c) Final resting position of swimmer.
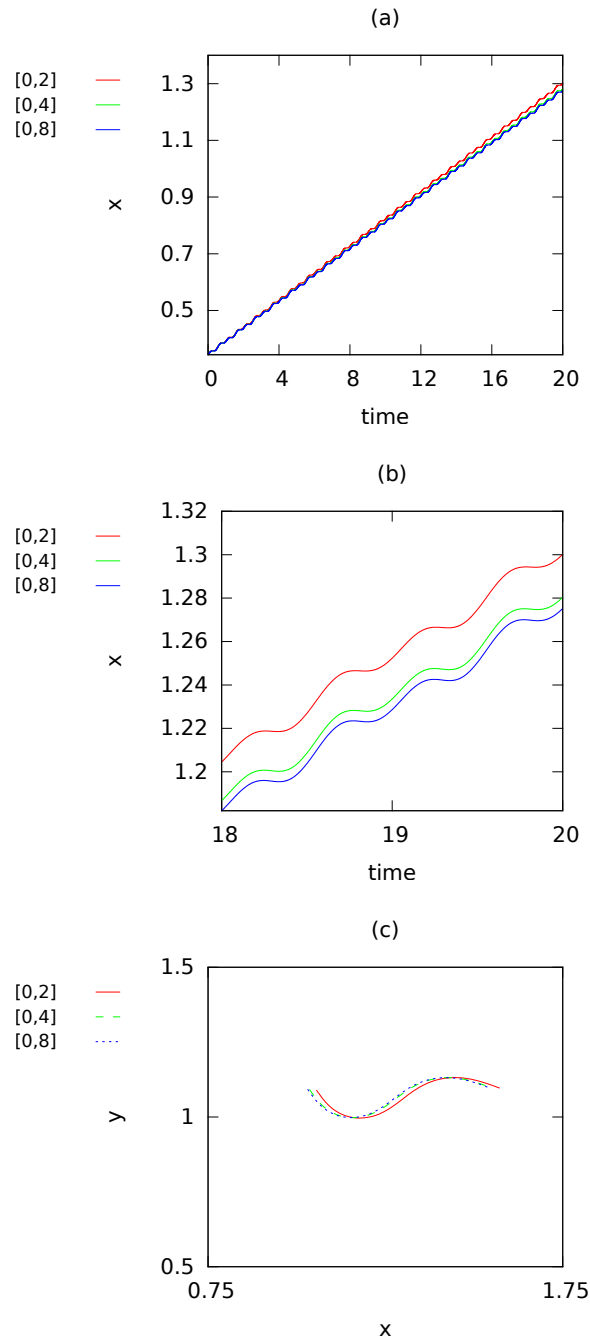
Figure 5.2: Effect of finite domain size on Newtonian ($De = 0$) burrower for domain sizes listed in Table 5.1. (a) location of center of mass throughout 20 periods, (b) location of center of mass during final 2 periods, (c) Final resting position of swimmer.
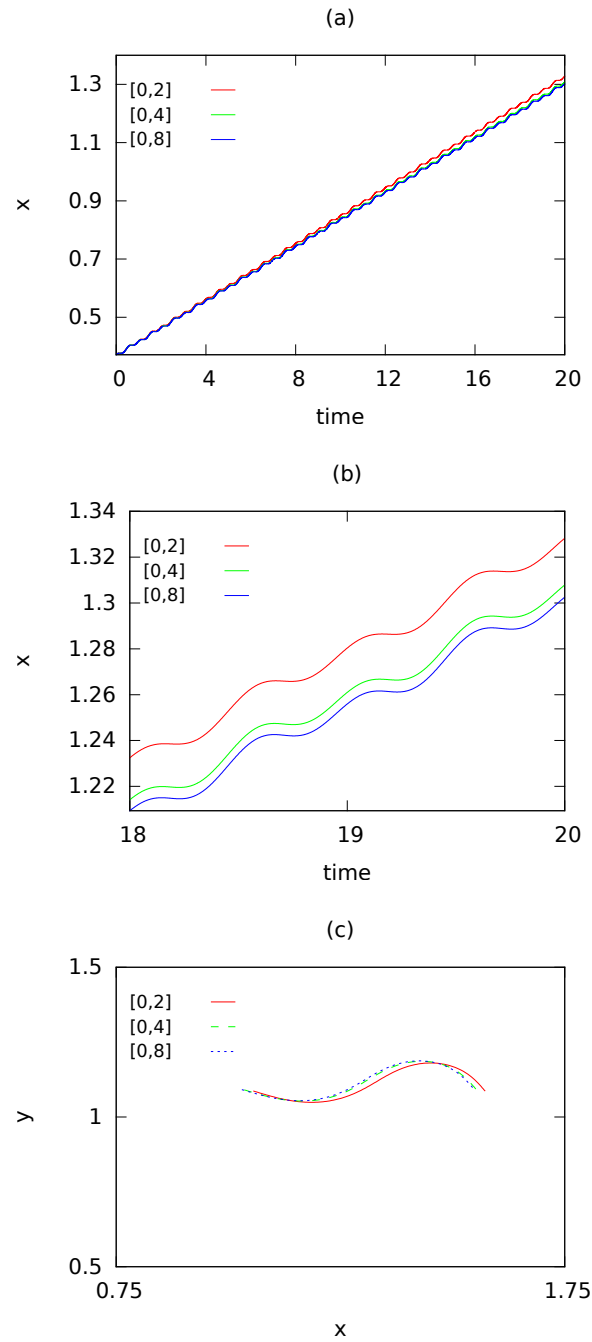
Figures 5.1 and 5.2 present a plot of the mean x position of the swimmer as a function of time for the three domains considered, as well as the final resting position of the swimmers. Note that there is an appreciable difference between the $[0, 2] \times [0, 2]$ and the $[0, 8] \times [0, 8]$ results ($\approx 2\%$); for the smaller domain, the locomotion of the swimmer is clearly affected by that of the periodic images. The difference between the $[0, 4] \times [0, 4]$ and the $[0, 8] \times [0, 8]$ results is not as significant ($< 0.5\%$), and to better afford the required high resolution for the viscoelastic simulations, we will now fix the computational domain to be $[0, 4] \times [0, 4]$.

5.1 Resolution and Enforcement of the Constraints

We now perform a resolution study for the kicker and burrower with $De = 0$ and $De = 5$. The rest of the parameters are again as in Table 5.2. The spatial resolutions used are defined by $\Delta x = 2^{-6}$, $\Delta x = 2^{-7}$ and $\Delta x = 2^{-8}$ for domain $\Omega = [0, 4] \times [0, 4]$. Figure 5.3 displays the mean x position of the swimmer as a function of time for the three numerical resolutions. The figure shows convergence of the swimmer's mean displacement as the resolution is increased. The lower resolutions significantly underestimate the swimmers mean displacement.
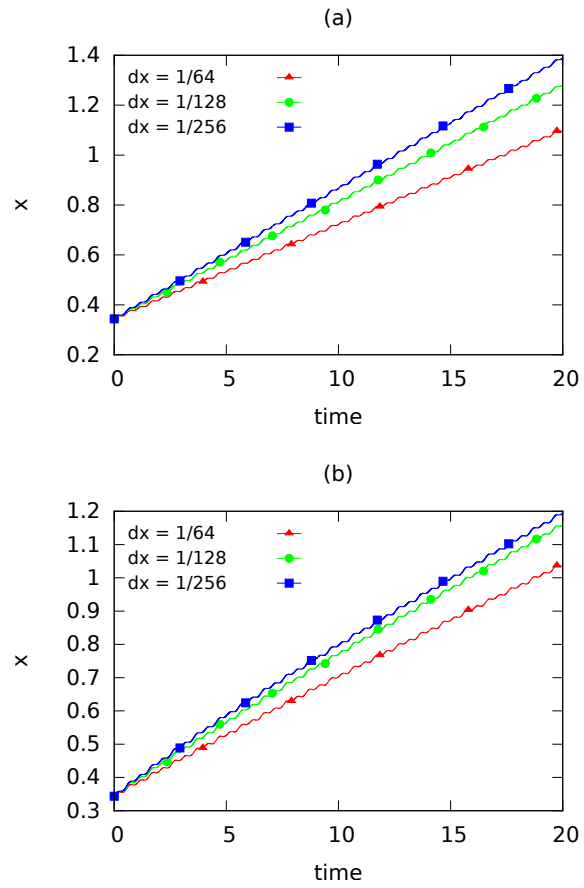
Figure 5.3: Kicker's mean x position for $\Delta x = 2^{-6}, 2^{-7}, 2^{-8}$. (a) corresponds to $De = 0$ and (b) corresponds to $De = 5$. The mean propulsion speed is significantly underestimated by the lower resolutions.
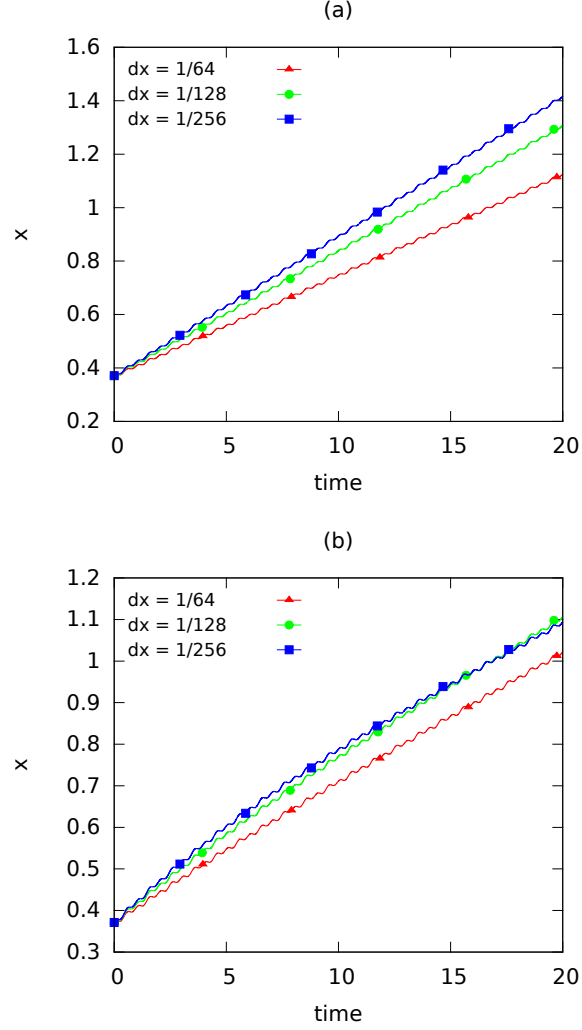
Figure 5.4: Burrower's mean x position for $\Delta x = 2^{-6}, 2^{-7}, 2^{-8}$. (a) corresponds to $De = 0$ and (b) corresponds to $De = 5$. The mean propulsion speed is significantly underestimated by the lower resolutions.

We now vary S_2 keeping all other parameters fixed (as in Table 5.2 with $\Delta x = 2^{-8}$). Recall that the value of S_2 effectively determines how strongly the given gait is imposed. Figures 5.5 and 5.6 show the mean x position of the swimmers (Stokesian and $De = 5$) as a function of time for various values of S_2. We observe

37

convergence of the swimmer's mean x position as S_2 is increased. In particular, tables 5.3 and 5.4 show that the number of grid points (for both kicker and burrower, $De = 1$) that deviate more than 10% from the target curvature is $\approx 1\%$ for $S_2 = 10^4$, and $\approx 4\%$ for $S_2 = 10^3$.

Figure 5.5: Kicker's mean x position for $S_2 = 2, 10^1, 10^2, 10^3, 10^4$. (a) corresponds to $De = 0$ and (b) corresponds to $De = 5$.

$S_2 =$	2	10	10^2	10^3	10^4
$\left\| \bar{\kappa} - \kappa \right\|_{l_\infty}$	9.08	2.07	0.73	0.09	0.04
$\frac{\text{count} \left| \frac{\bar{\kappa} - \kappa}{\bar{\kappa}} \right| > .1}{N_b}$	0.94	0.82	0.30	.04	0.01

Table 5.3: (Kicker) Percent deviation from the target curvature for various values of S_2 and $De = 1$. Additionally, the last row includes percentage of Lagrangian grid points that deviate more than 10 percent from the target curvature.
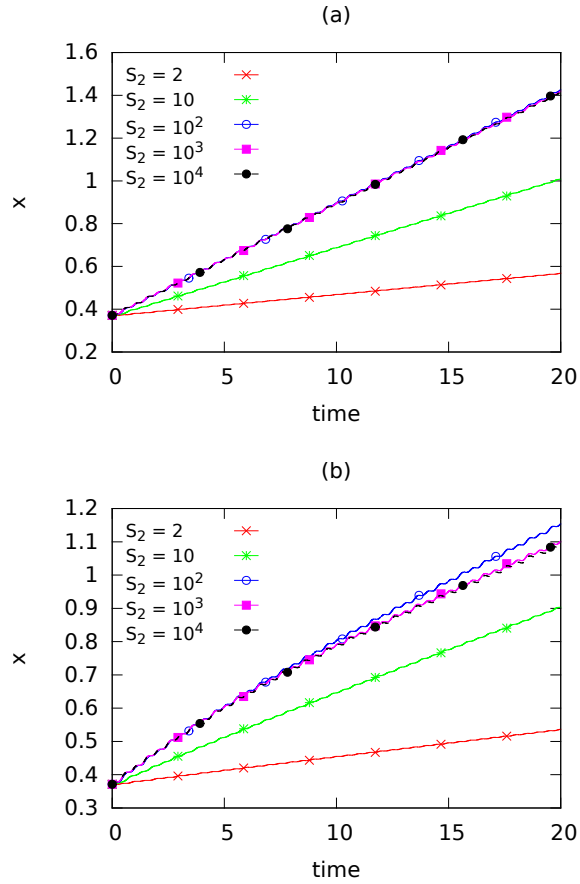
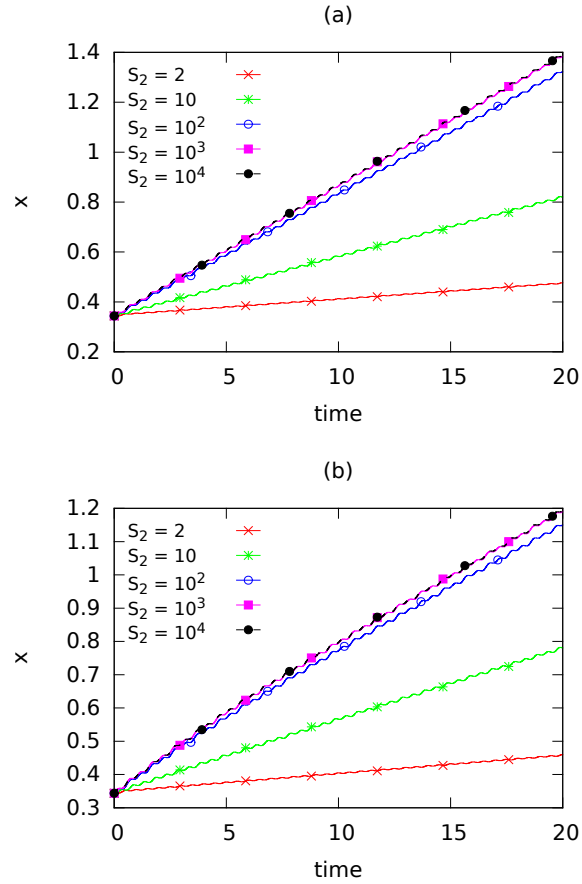**Figure 5.6:** Burrower's mean x position for $S_2 = 2, 10^1, \ 10^2, \ 10^3, \ 10^4$. (a) corresponds to $De = 0$ and (b) corresponds to $De = 5$.

$S_2 =$	2	10	10^2	10^3	10^4
$\left\lVert \bar{\kappa} - \kappa \right\rVert_{l_\infty}$	6.90	3.28	0.84	0.10	0.02
$\frac{\text{count} \left\lvert \frac{\bar{\kappa} - \kappa}{\bar{\kappa}} \right\rvert > .1}{N_b}$	0.90	0.74	0.33	.04	0.01

Table 5.4: (Burrower) Percent deviation from the target curvature for various values of S_2 and $De = 1$. Additionally, the last row includes percentage of Lagrangian grid points that deviate more than 10 percent from the target curvature.
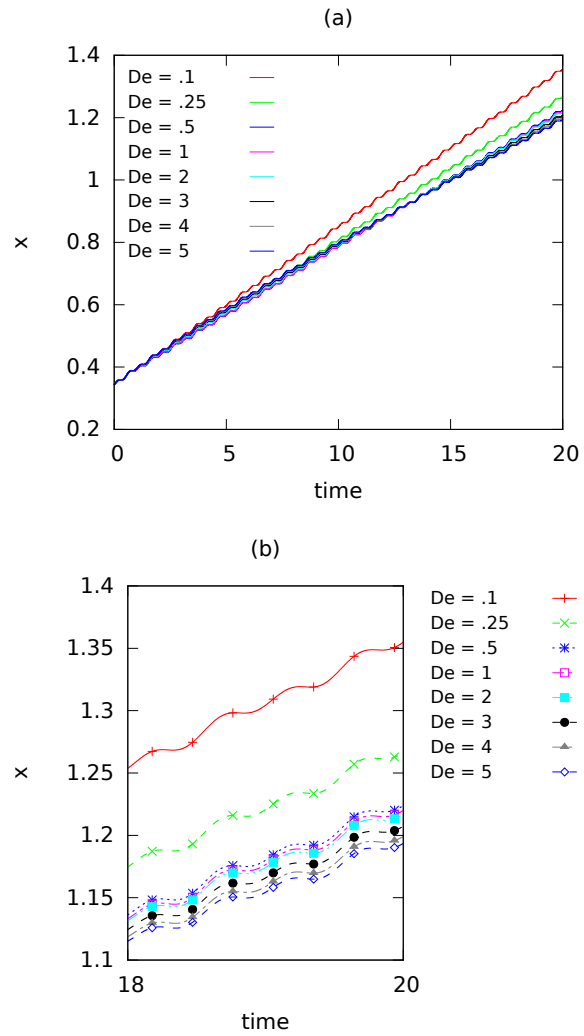
5.2   Inextensible Swimmer

We now look at the dynamics of the finite swimmer for different Deborah numbers. Based on the resolution study presented earlier, we fix $\Delta x = 2^{-8}$ and set all the other parameters as in Table 5.2 (except for De which will be varied). Note the high values $S_1 = 10^7$ and $S_2 = 10^4$ used to guarantee an accurate enforcement of both the inextensibility constraint and the gait, where S_1 is chosen large enough relative to S_2 to ensure the swimmer does not break. The use of such large stiffness parameter was made possible by the semi-implicit IB method [5].

Figures 5.7, 5.8 and 5.9 show a clear monotonic ordering of the fixed gait swimmers' mean displacement and velocity with respect to De (after 20 periods). Indeed, the steady state mean locomotion speed of the swimmer decreases with an increase in De. Before reaching steady state, however, there is a period of time ($\approx t < 3$, see Figure 5.9) during which the mean velocities of the swimmers are inversely related to the Deborah number. This is an effect of the faster beating pattern, or larger relaxation times associated with larger Deborah numbers.

Figure 5.7: Mean x position of fixed gait kickers versus time for various De. There is a monotonic decrease in mean x position with De.
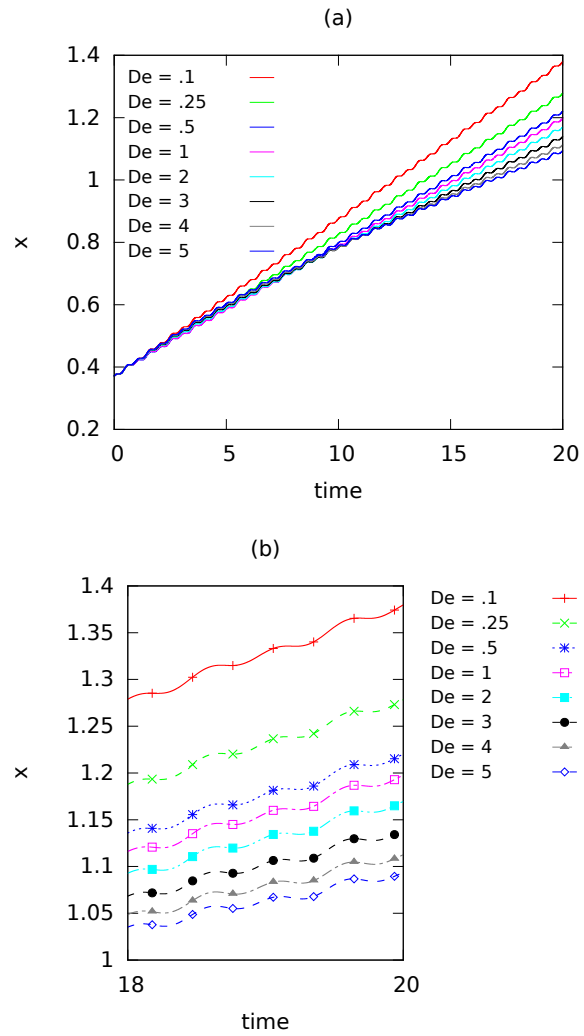
Figure 5.8: Mean x position of fixed gait burrowers versus time for various De. There is a monotonic decrease in mean x position with De.
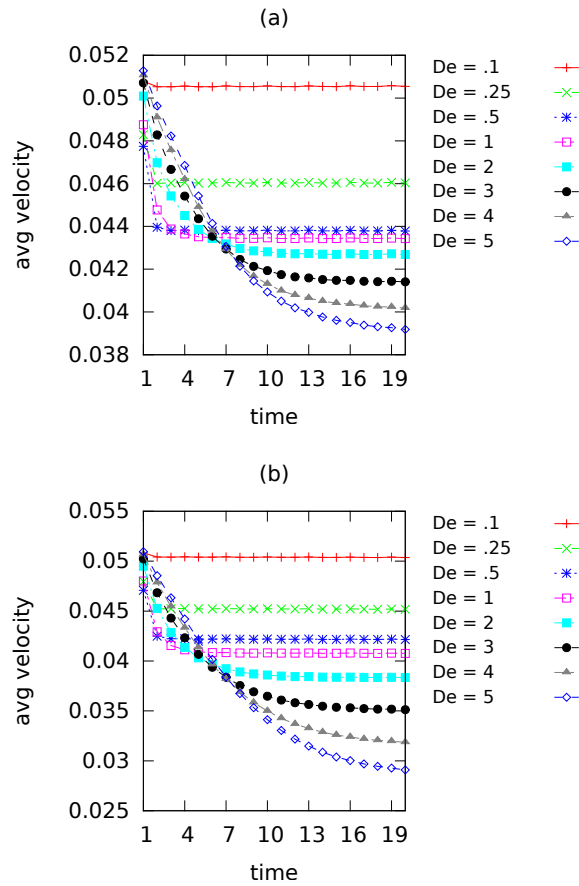
Figure 5.9: Average velocity versus period for various De. (a) Kicker, (b) Burrower.

5.3 Flexible Swimmers and Effects of Stress Dissipation

In light of the varying theoretical, experimental and numerical results [9, 32, 34, 27], we further explore the effects of varying the S_2 parameter, as well as adding stress dissipation to the Oldroyd-B constitutive equation. We begin by varying S_2 and setting all other parameters as in Table 5.2. Recall that S_2 determines

how strongly the gait is enforced. Figure 5.10 shows the Newtonian-normalized final velocity (after 20 periods) for various S_2 values. Here the final velocities are computed by averaging the forward propulsion of the swimmer's center of mass throughout the final period. Notably, we see that if the gait enforcement is relaxed enough (S_2) there is a reversal of the steady state ordering found in Figure 5.9, but no speed-up relative to the Newtonian swimmer.
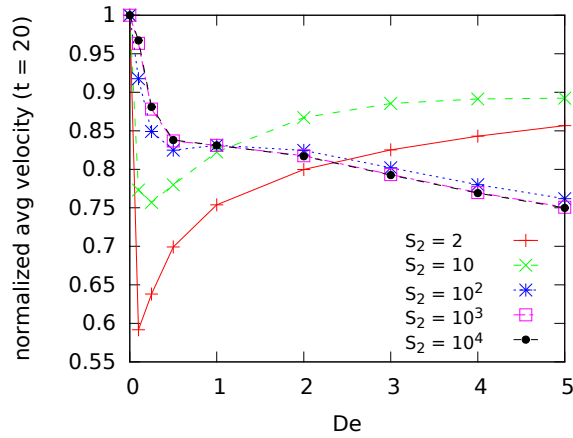
Figure 5.10: Newtonian-normalized velocities after 20 periods versus De for various S_2.

Next we consider the effects of adding stress dissipation to eq. (2.20). Recently Thomasses and Shelley [35] numerically demonstrated the possibility of finite-time blow up in the stresses for the Oldroyd-B model. In [33] Thomasses found that adding $\delta = O(h)$ stress dissipation is sufficient to mitigate this growth. In light of these results, it is tempting to rewrite the Oldroyd-B constitutive equation as

$$\boldsymbol{\tau}_p + De\,\boldsymbol{\tau}_p{}^{\nabla} = \epsilon\left[\nabla\mathbf{u} + \nabla\mathbf{u}^T\right] + \delta\Delta\boldsymbol{\tau}_p. \tag{5.8}$$

44

In this form, eq. (5.8) not only ensures finite polymeric stresses, but allows for the advective term to be discretized with a standard second order central difference scheme. To explore the effects of adding of stress dissipation, we set $\Delta x = 1/128$, $\Delta t = .3\Delta s$ and maintain the domain $\Omega = [0, 4] \times [0, 4]$. All other parameters are as in table 5.2 and first-order upwinding is used to compute the advective term, except where noted.

In Figure 5.11 we plot the Newtonian-normalized mean velocity of the kickers, averaged over the final period, as a function of Deborah number, and for various dissipation coefficients, δ. Notably, setting $\delta = 1.28h = .01$ results in an enhancement of the mean swimming velocity. In particular, the viscoelastic swimmers are all faster than their Newtonian counterpart. While similar numerical results have been found in [32, 34], they attributed it to the combined gait asymmetry and swimmer elasticity. Comparing the first-order upwind scheme ($\delta = 0$) and third-order ENO results, we see the effect of numerical stress dissipation introduced by the upwind scheme. Moreover, when the stresses are appropriately resolved (as with the third order ENO results in Figure 5.11), we see the hint of a limiting, minimal locomotion speed as $De \to \infty$. It is however, extremely challenging to capture this apparent limit numerically as larger De become computationally formidable.

Figure 5.12 shows a plot of the mean-square polymer extension, $Tr(\langle \mathbf{Q} \otimes \mathbf{Q} \rangle_\psi)$, at $t = 20$. The figure serves to further emphasize the side effects that the addition

of stress dissipation may have on results. The effects when $\delta = .01$ $(O(h))$ are remarkable, and again we see the discrepency between the third order ENO scheme and first order upwinding.
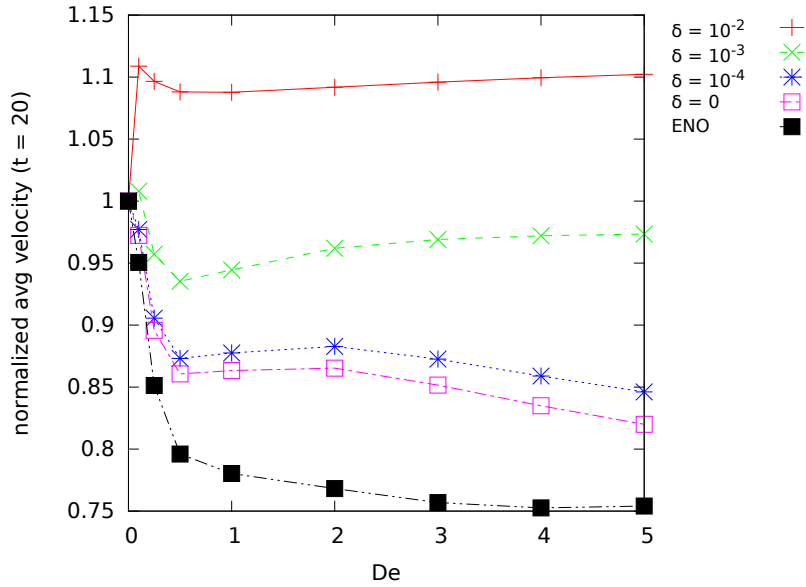
Figure 5.11: Newtonian-normalized velocities after 20 periods, versus De, and for various stress dissipation coefficients, δ and $S_2 = 10^4$. Note the difference between the first-order upwind and third-order ENO results.
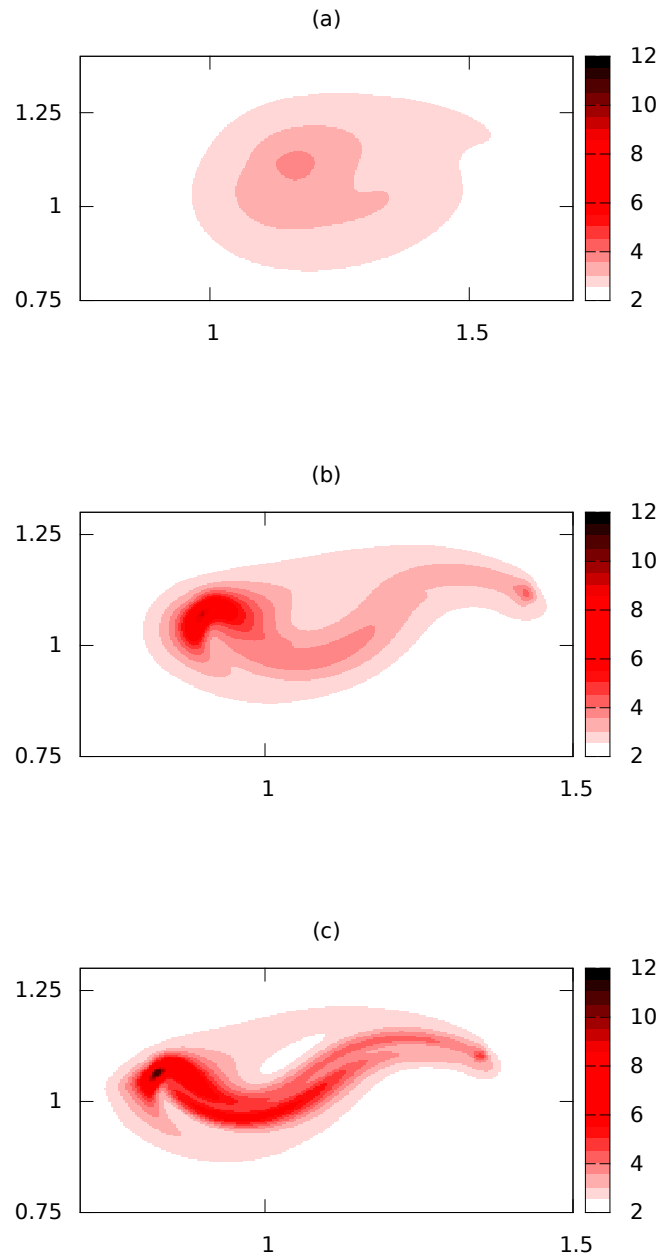
Figure 5.12: Measure of mean square polymer extension, $Tr(\langle \mathbf{Q} \otimes \mathbf{Q} \rangle_\psi)$, at $t = 20$ for $De = 1$. (a) $\delta = .01$, (b) first-order upwinding, (c) third-order ENO.

Chapter 6

Adaptive Multiresolution Scheme

As previously noted in Chapter 4, the Oldroyd-B model can lead to finite-time blow up in the stresses and is best suited for modeling simple Boger fluids [15]. For example, Figures 6.1 and 6.2 show the evolution of the $xx-$component of the polymeric stress tensor in extensional flow for both the Oldroyd-B and FENE model. For the case of fixed extensional flow $\mathbf{u} = (x, -y)$ and $De = 0.1$ the stress remains bounded and we observe convergence of the FENE stress to the Oldroyd-B stress as the extensibility parameter in the FENE model is increased. However, increasing the Deborah number to $De = 0.5$ (which corresponds to larger polymeric relaxation times or increased flow rate) results in divergence of the Oldroyd-B stress, while the FENE results remain bounded and converge to steady state.
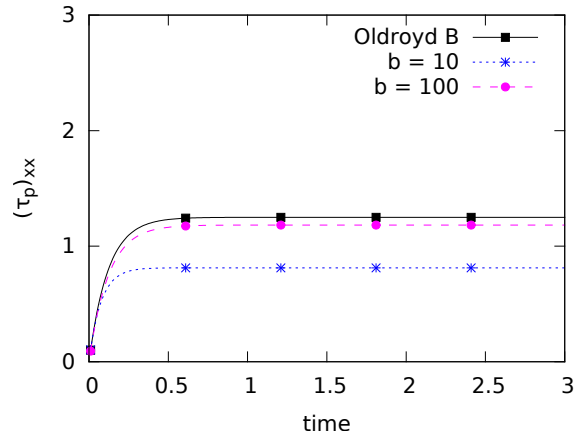
Figure 6.1: $(\boldsymbol{\tau}_p)_{xx}$ for planar extensional flow $\mathbf{u} = (x, -y)$ and $De = .1$ using Oldroyd-B and FENE models.
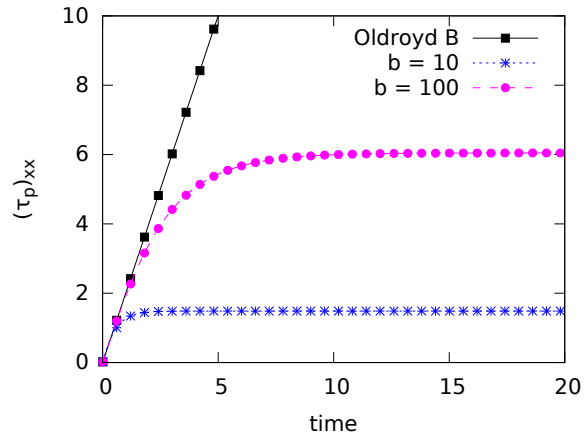
Figure 6.2: $(\boldsymbol{\tau}_p)_{xx}$ for planar extensional flow $\mathbf{u} = (x, -y)$ and $De = .5$ using Oldroyd-B and FENE models. Note the divergence of the Oldroyd-B stress.

The major benefits of employing the FENE model is that it ensures the finite extensibility of the polymer dumbbells and agrees better with experimental results [2]. However, the same nonlinear (intramolecular) force that enusures finite extensibility also prohibits any closure approximations of the coupled system

(2.10)-(2.11). In this section we introduce an adaptive multiscale methodology that makes it feasible to compute the viscoelastic stresses using the FENE model.

To mitigate the computational difficulties introduced by the higher dimensionality of the model, we will employ an adaptive multiresolution technique on the spectral coefficients, α, which are evolved via equations (3.33)-(3.34):

$$\frac{\alpha^* - \alpha^n}{\Delta t} = -(\kappa_{11} + \kappa_{22})\alpha^n + b_1 L_1 \alpha^n - b_2 \frac{d\alpha}{d\theta}^n + L_0 \alpha^*$$

$$\frac{\alpha^{n+1} - \alpha^*}{\Delta t} = -\mathbf{u}^n \cdot \nabla \alpha^*.$$

A multiresolution scheme represents data on a series of nested grids, each dyadically finer than the previous one, and in such a way that the information on the finer grids can be completely recovered from the coarser ones. Such schemes were pioneered by Harten [13, 14] and have been successfully used for the adaptive computation of fluxes in hyperbolic and parabolic equations in conservation form [14, 26, 25].

For microscopic swimmers, the viscoelastic stresses are highly localized in the region along the swimmer (see Figure 5.12), and moreover, this is the region where α will vary the most as a function of the spatial variable $\boldsymbol{x}$. We will exploit this fact in our use of the multiresolution analysis.

To demonstrate the idea of multiresolution analysis, we first consider the periodic scalar function f defined on the interval $[0, 1]$. Let

$$\{x_i^l\}_{i=0}^{N_l-1}, \ \ N_l = 2^l, \ \ h_l = 2^{-l}, \ \ x_i^l = i \cdot h_l \tag{6.1}$$

be a discretization of $[0, 1]$. Then, a dyadic refinement of this grid would correspond to

$$\{x_i^{l+1}\}_{i=0}^{N_{l+1}-1}, \ \ N_{l+1} = 2^{l+1}, \ \ h_{l+1} = 2^{-l-1}, \ \ x_i^{l+1} = i \cdot h_{l+1}. \tag{6.2}$$

Letting $f_j^m = f(x_j^m)$, then $f_j^l = f_{2j}^{l+1}$, since $x_j^l = x_{2j}^{l+1}$. Note that $x_{2j+1}^{l+1} \in [x_j^l, x_{j+1}^l]$ (see Figure 6.3).
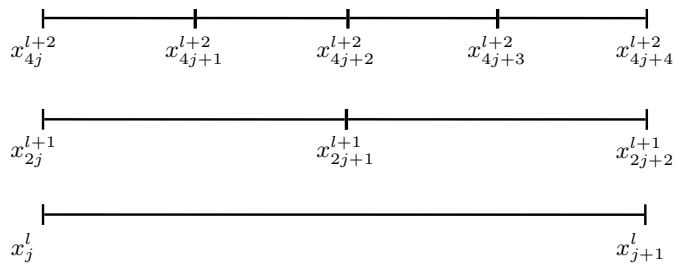

Figure 6.3: Example of dyadic grid refinement

If we let $\mathcal{I}(f)^{l+1}_{2j+1}$ be an approximation to f^{l+1}_{2j+1} derived from the values on the coarser grid corresponding to l, then we can write

$$f^{l+1}_{2j+1} + d^l_j = \mathcal{I}(f)^{l+1}_{2j+1} \tag{6.3}$$

where d^i_j is the error produced by the approximation. We refer to d^i_j as the (multiresolution) *details*. For a fixed approximation operator, $\mathcal{I}$, the information provided by the function values on the grid corresponding to $l+1$,

$$\{f^{l+1}_i\}^{N_{l+1}-1}_{i=0}, \tag{6.4}$$

is exactly the same as the function values on the coarser grid (l) coupled with the details,

$$\{d^l_i, f^l_i\}^{N_l-1}_{i=0}. \tag{6.5}$$

While the two formulations in (6.4) and (6.5) are identical, the details in (6.5) provide a measure of the local regularity of the function which will be leveraged to derive adaptive strategies.

6.1 Adaptive Multiscale Algorithm and Tree Data Structure

We begin by considering the collection of nested grids defined on $[a, b]$:

$$\left\{ \{x_j^l\}_{j=0}^{N_l-1} \right\}_{l=1}^{L}, \quad x_j^l = j \cdot h_l, \quad h_l = \frac{h_0}{2^l}, \quad N_l = \frac{b-a}{h_l}. \tag{6.6}$$

From the previous section we have that for any periodic scalar function defined on $[a, b]$,

$$\left\{ \{f_j^l\}_{j=0}^{N_l-1} \right\}_{l=0}^{L} = \left\{ f^0, d^0, \ldots, d^L \right\}, \tag{6.7}$$

with the details providing a measure of the local regularity of the function. The idea is to use the details to dynamically determine the appropriate local level of resolution, and adapt it at each time-step. Implenting the method efficiently requires the use of a tree data structure. In this case we will make use of the dynamic tree and algorithm presented in [26, 25].

To illustrate the main idea of the method, we begin with an example in one-dimensional space using three progressively (and dyadically) finer grids. Let f be the scalar function defined in Figure 6.4.
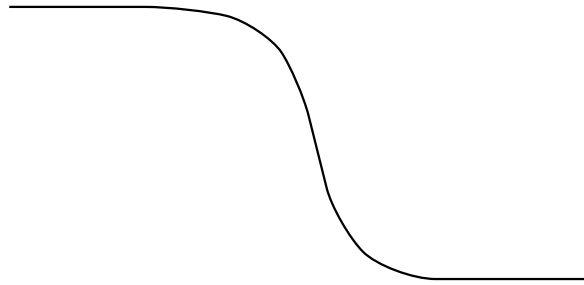
Figure 6.4: One-dimensional scalar function with sharp transition.

Figure 6.5 illustrates how a fine grid manages to resolve the steep gradient in the function while over resolving the smooth regions. Here the circles represent equally spaced grid points, also referred to as *nodes* from here on out.

Figure 6.5: One-dimensional scalar function defined over a fine grid.

Instead of using one grid to represent the function, we consider the nested grids $\mathcal{G}^0 \subset \mathcal{G}^1 \subset \mathcal{G}^2$ (see Figure 6.6).
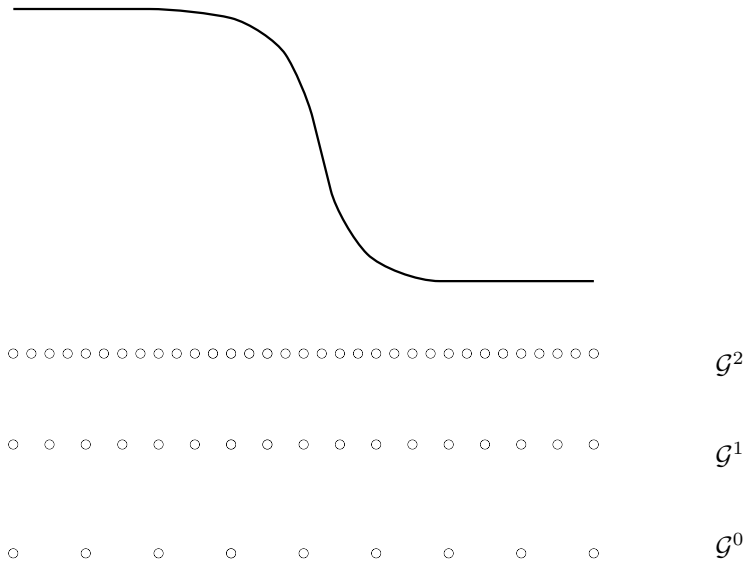
Figure 6.6: One-dimensional scalar function defined over three dyadically finer and nested grids.

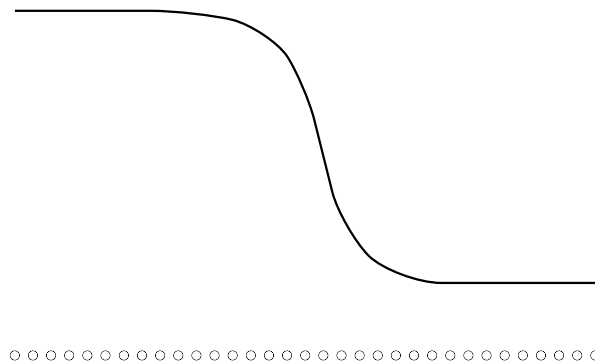The goal is to systematically determine the appropriate grid $\mathcal{G}^l$, $l = 0, 1, 2$ to locally represent the function. This is dependent on the choice of interpolation, $\mathcal{I}$, and detail (error) tolerance, δ. Starting from the coarsest grid $\mathcal{G}^0$ we compare the function values on the next grid ($\mathcal{G}^1$, which is finer), with the interpolated values determined from $\mathcal{G}^0$. For example, let f_i^0 be the function value on $\mathcal{G}^0$ defined at x_i^0. Then, as noted before $x_{2i}^1 = x_i^0$ and $x_{2i+1}^1 \in (x_i^0, x_{i+1}^0)$ as illustrated in Figure 6.7.
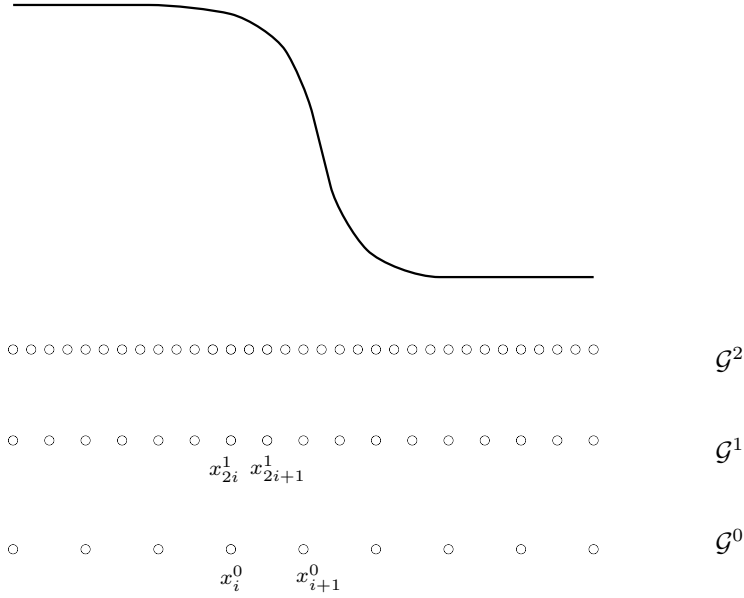
Figure 6.7: Illustration of the nested nature of the grids: $x^1_{2i+1} \in (x^0_i, x^0_{i+1})$. Note that $\mathcal{G}^0 \subset \mathcal{G}^1 \subset \mathcal{G}^2$.

We now compare the value interpolated using $\mathcal{G}^0$ and the actual value on $\mathcal{G}^1$,

$$|\mathcal{I}(f)^1_{2i+1} - f(x^1_{2i+1})| < \delta. \tag{6.8}$$

If we were using linear interpolation, then eq. (6.8) would read

$$\left| \frac{1}{2} \left(f^0_i + f^0_{i+1} \right) - f(x^1_{2i+1}) \right| < \delta. \tag{6.9}$$

If the inequality is satisfied, then we mark the point x^0_i, indicating that $\mathcal{G}^0$ is sufficient to resolve the function within the given tolerance at this point. If the inequality is not satisfied, then we perform the same comparison using x^1_{2i}, x^1_{2i+1}

56

and the associated values on $\mathcal{G}^2$. Note that since $x_i^0 = x_{2i}^1$, $f_i^0 = f_{2i}^1$ and thus they do not need to be compared.

After the multiresolution analysis is complete, the tree might look something like Figure 6.8. We emphasize that the function values at the unmarked nodes (empty circles) in the finest grid, $\mathcal{G}^2$, can be recovered from the coarser grids using the predefined interpolation operator, $\mathcal{I}$, and to within a controlled tolerance by decreasing δ.
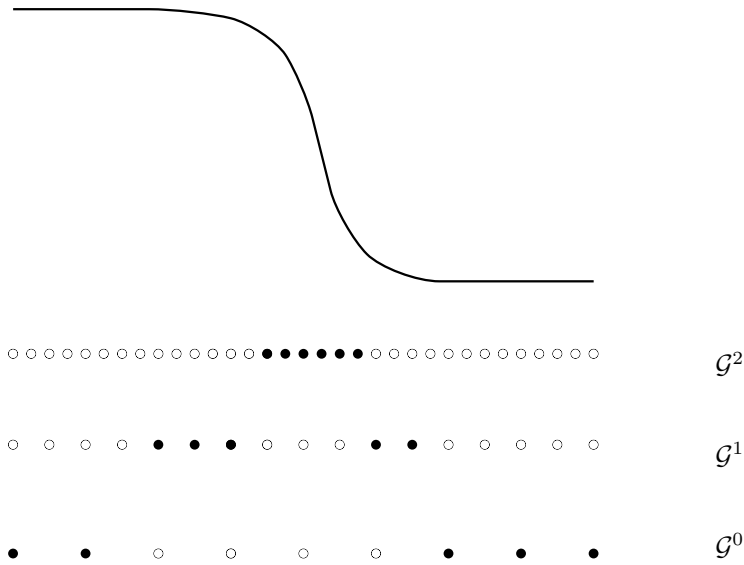
Figure 6.8: Marked nodes after multiresolution analysis has been performed. Note that the finest grid is only marked near the sharp transition of the function.

In the context of the data structure, the tree is represented by Figure 6.9, where the black lines in the figure are representative of pointers, every circle is a node, and the filled circles are referred to as *leaves*. The coarsest grid is referred to as the *root*, and every non-root node has a *parent* and *siblings* (children of

the same parent). Each node in the tree is a data object that contains pointers to its siblings, cousins (children of parent's siblings), parent and children (where applicable). Additionally, a node contains the spectral coefficients, details, and stress tensor $\boldsymbol{\tau}_p$. The multiresolution methodology works by evolving the spectral coefficients on the leaves and using interpolation to recover the function values on the finest grid, $\mathcal{G}^2$, adding and removing nodes as necessary at each time step.
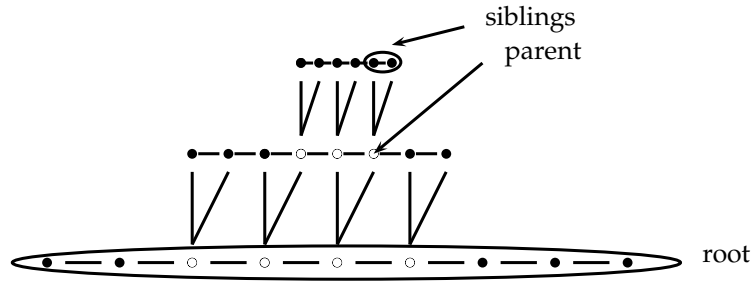
Figure 6.9: Grids in the context of the tree data structure. We refer to the coarsest grid as the *root*. Also, any non-root node has a *parent* and *siblings* (children of same parent).

The extension from one dimension to two, and even three, is natural and once again defined by dyadic refinement. The equivalent of (6.6) on the periodic domain $\Omega = [a, b] \times [c, d]$ is

$$\left\{ \mathcal{G}^l = \{(x_i, y_j)^l\}_{i,j=0}^{N_l^x - 1, N_l^y - 1} \right\}_{l=1}^{L} \tag{6.10}$$

$$x_i^l = i \cdot h_l^x, \quad h_l^x = \frac{h_0^x}{2^l}, \quad N_l^x = \frac{b - a}{h_l^x} \tag{6.11}$$

$$y_j^l = j \cdot h_l^y, \quad h_l^y = \frac{h_0^y}{2^l}, \quad N_l^y = \frac{d - c}{h_l^y}, \tag{6.12}$$

58

where the grids are nested:

$$\mathcal{G}^0 \subset \mathcal{G}^1 \subset \cdots \subset \mathcal{G}^L. \tag{6.13}$$

In what follows we briefly present the adaptive multiscale methodology for the spectral coefficients, α. For a more comprehensive review of multiresolution analysis the reader is referred to [13, 14, 1], and for an additional explanation of the algorithm the reader is encouraged to review [26, 25].

6.2   Multiresolution Algorithm

Given the tree and flow, $\mathbf{u}$, at time t_n, the algorithm proceeds as follows:

1. For each node in the root, navigate all the way to the leaves and compute α^* using eq. (3.35).

2. For each node in the root, navigate all the way to the leaves and compute α^{n+1} using eq. (3.34), interpolating where necessary. Also update the stress tensor $\boldsymbol{\tau}_p$ using Kramer's formula (2.10).

3. Starting at the leaves, project the node's updated values to the corresponding coarser grid nodes until the root is reached (recall that the grids are nested). Figure 6.10 shows this step in one dimension.
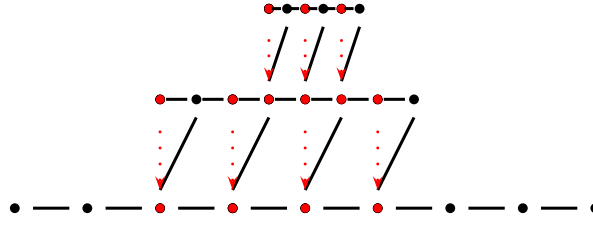
Figure 6.10: Projection step in adaptive multiresolution methodology.

4. Interpolate the stress tensor to the full spatial grid using the interpolation operator $\mathcal{I}$.

5. Starting at the root, update the details at every (non-root) node by using α and $\mathcal{I}(\alpha)$. Since the detail needs to be a scalar value and α is the spectral coefficient vector, we define the detail as $\|\alpha^{l+1} - \mathcal{I}(\alpha)^{l+1}\|_\infty$

6. By analyzing the details of every node, update the tree by splitting (adding) or removing nodes as necessary. Essentially, nodes are added in regions where there are leaves with details greather than δ, and nodes are deleted in regions where there are leaves with details smaller than δ.

7. Using the updated stress tensor $\boldsymbol{\tau}_p$ (defined on the entire spatial grid), update the flow variables (and swimmer) and go back to the first step.

6.3   Multiresolution Validation

We now perform convergence studies for both the multiresolution scheme tolerance, δ, and the spectral grid. For these tests we use 4 multiresolution grids, with the coarsest defined by $\Delta x = 2^{-5}$ and the finest by $\Delta x = 2^{-8}$, which corresponds with the full spatial grid. The interpolation, $\mathcal{I}$, used for the details and recovery of the stress is a three point centered stencil in each dimension (centered at the node's parent). For the swimmer we use an inextensible small amplitude kicker governed by

$$\bar{\kappa}(s,t) = -A(s-L)k^2 \sin(ks + \omega t), \quad s \in [0, L], \tag{6.14}$$

with $A = 0.05$ and $\Omega = [0,2] \times [0,2]$. The spatial resolution is set to $\Delta x = 2^{-8}$, $\Delta s = 0.5\Delta x$, the time step to $\Delta t = 0.5\Delta s$, and $S_2 = 10^5$.

Recall that we perform the multiresolution analysis on the spectral (probability distribution function) coefficients which are evolved in time via (3.35). For $De = 1$ and $De = 2$, we first set $(N_f, N_r) = (8,8)$ and vary the multiresolution tolerance. Then we fix the error tolerance and vary the spectral resolution. We plot the L_1 norm of the difference in successive stress tensor components as the tolerance and spectral resolution are varied.

Figures 6.11 and 6.13 show the convergence of the stress tensor as the tolerance, δ, and spectral resolution are varied. Furthermore, Figure 6.12 shows the

convergence of the swimmer's center of mass throughout four periods (for varied tolerance). The plots show that for $De = 1$, $(N_f, N_r) \geq (6, 6)$ and $\delta \leq 10^{-5}$ are sufficient to resolve the viscoelastic stresses, with subsequent refinements of (N_f, N_r) and δ resulting in a change of $O(10^{-5})$ (in the L_1 norm), which is smaller than the first-order temporal discretization error, $O(10^{-4})$.

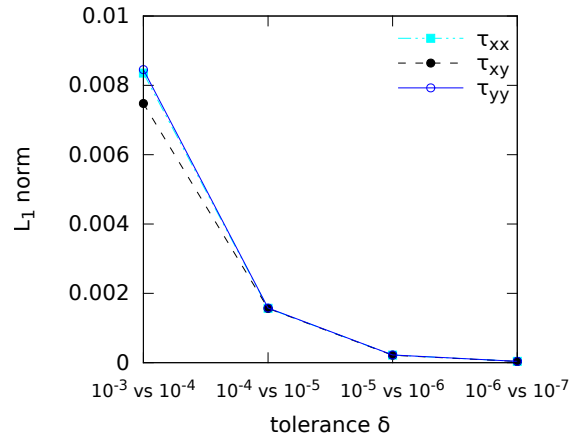**Figure 6.11:** $\left\| \boldsymbol{\tau}_p \left(\delta = 10^{-n} \right) - \boldsymbol{\tau}_p \left(\delta = 10^{-(n+1)} \right) \right\|_{L_1}$ for $n = 3, 4, 5, 6$, $De = 1$ and $(N_f, N_r) = (8, 8)$.
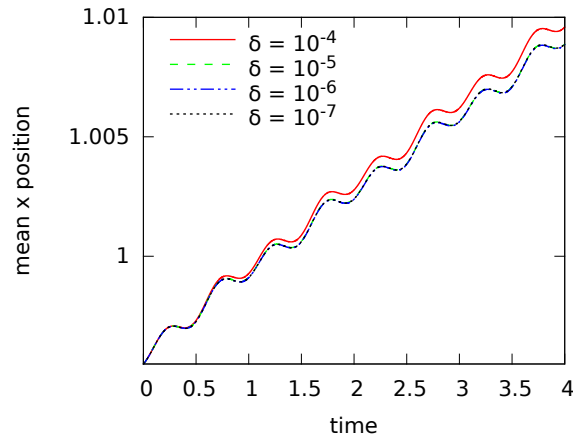

Figure 6.12: Kicker's center of mass through four periods for various multiresolution error tolerances, δ, $De = 1$ and $(N_f, N_r) = (8, 8)$

Figure 6.13: $\|\boldsymbol{\tau}_p\left(N_f, N_r\right) - \boldsymbol{\tau}_p\left(N_f + 1, N_r + 1\right)\|_{L_1}$ for $(N_f, N_r) = (4, 4), (5, 5), \ldots, (9, 9)$, $De = 1$ and $\delta = 10^{-5}$.

Next we perform the same tests for $De = 2$. The results can be found in Figures 6.14 through 6.16. In this case the spectral resolutions $(3, 3)$ and $(4, 4)$ are no longer sufficient to resolve the dynamics and, in fact, lead to instability. However, $\delta \leq 10^{-5}$ and $(N_f, N_r) \geq (6, 6)$ remain sufficient to accurately resolve the viscoelastic stresses, once again producing a difference of $O(10^{-5})$ in subsequent refinements.
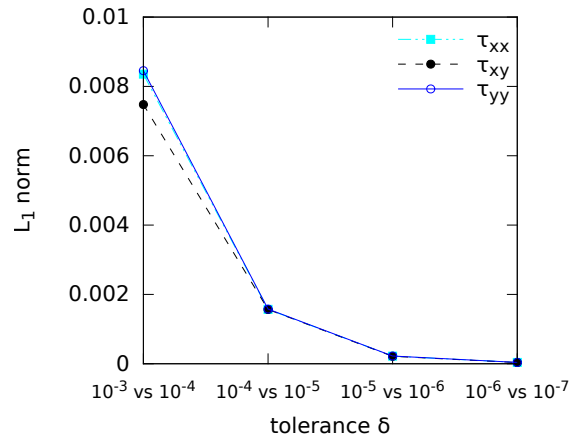
Figure 6.14: $\left\|\boldsymbol{\tau}_p\left(\delta=10^{-n}\right)-\boldsymbol{\tau}_p\left(\delta=10^{-(n+1)}\right)\right\|_{L_1}$ for $n=3,4,5,6$, $De=2$ and $(N_f,N_r)=(8,8)$.

Figure 6.15: Kicker's center of mass through four periods for various multiresolution error tolerances, δ, $De=2$, and $(N_f,N_r)=(8,8)$
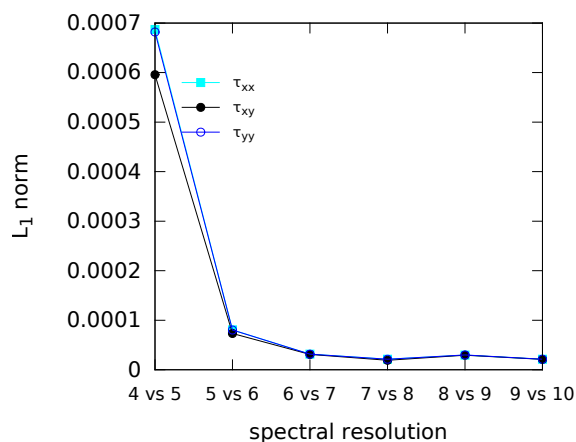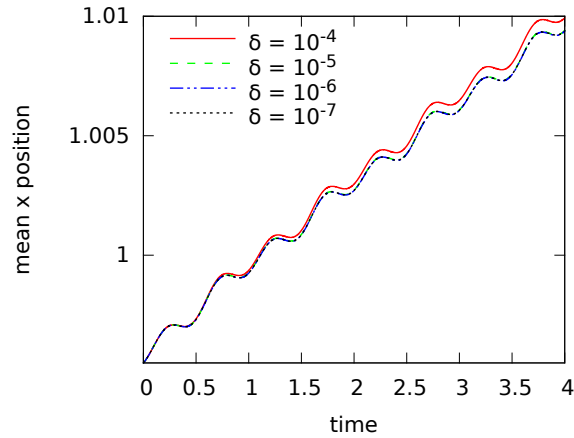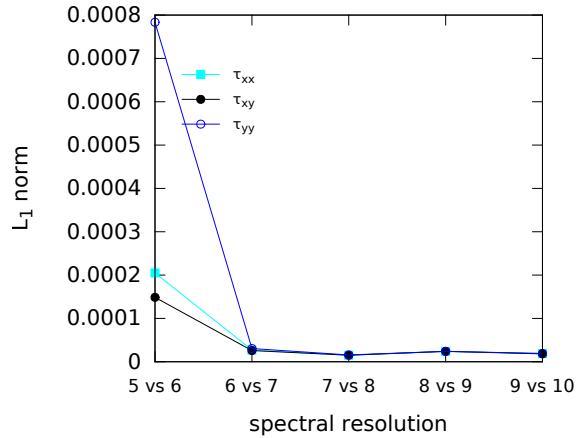
Figure 6.16: $\left\| \boldsymbol{\tau}_p \left(N_f, N_r \right) - \boldsymbol{\tau}_p \left(N_f + 1, N_r + 1 \right) \right\|_{L_1}$ for $\left(N_f, N_r \right) = (4, 4), (5, 5), \ldots, (9, 9)$, $De = 2$ and $\delta = 10^{-5}$.

6.4 Multiresolution Perfomance

Next, we analyze the multiresolution methodology's perfomance for various tolerances. Based on the results of Section 6.3, we set $De = 1$ and the spectral resolution to $(N_f, N_r) = (8, 8)$. Figure 6.20 shows the number of leaves in the tree after 4 periods as a function of the error tolerance. In particular, the grid corresponding to $\delta = 10^{-5}$ has approximately 6.6 times fewer grid points than the $\delta = 0$ grid (full grid). These results are visualized in Figures 6.18 and 6.19. In these figures every grid point is representative of a leaf in the tree data structure.
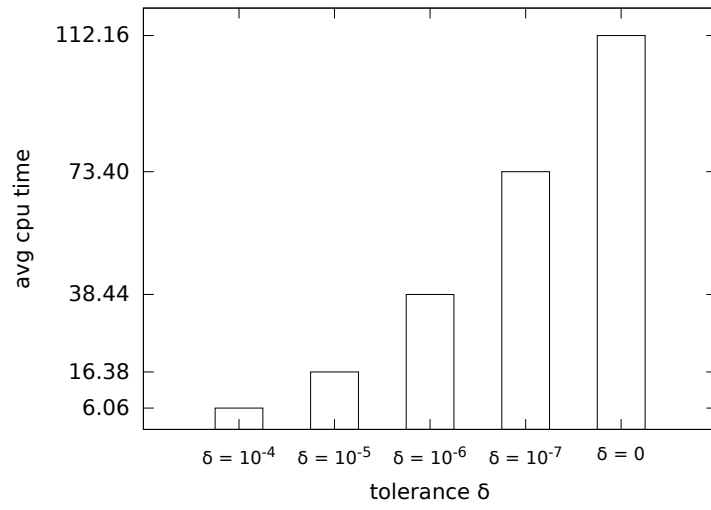
Figure 6.17: Average cpu time through $t = 4$ as the tolerance is decreased.
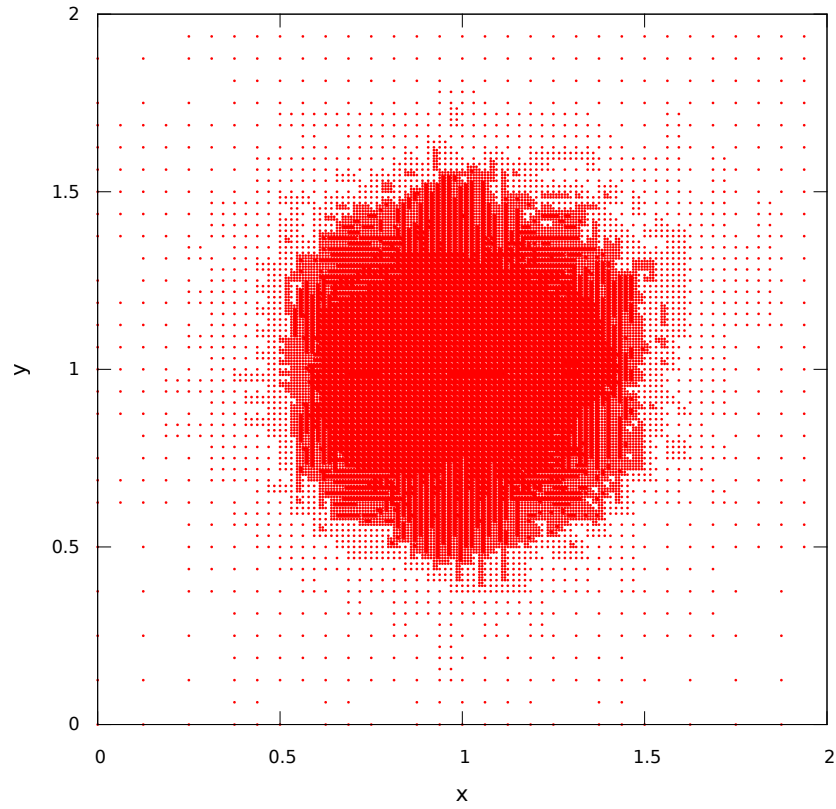
Figure 6.18: Leaves after 4 periods of small amplitude kicker in a FENE fluid simulation. Four multiresolution grids were used and $De = 1$.

Figure 6.19: Close-up of the concentration of leaves in Figure 6.18.

Given that there is computational overhead introduced by the multiresolution analysis, we now look at the differences in cpu-time for various error tolerances, δ. Figure 6.17 contains the average cpu-time (averaged over the 4 periods) as a function of error tolerance. We see from the figure that the multiresolution

simulations with $\delta = 10^{-5}$ are approximately 6.8 times faster than the $\delta = 0$ (full grid) case.
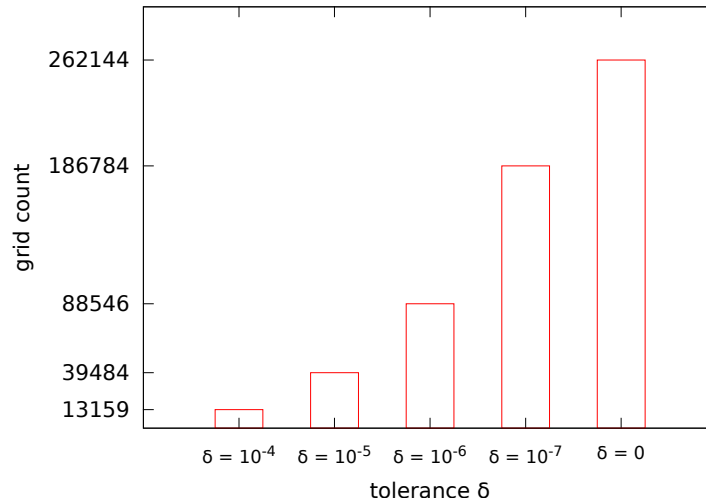
Figure 6.20: Total number of leaves (at $t = 4$) as the error tolerance δ is decreased.

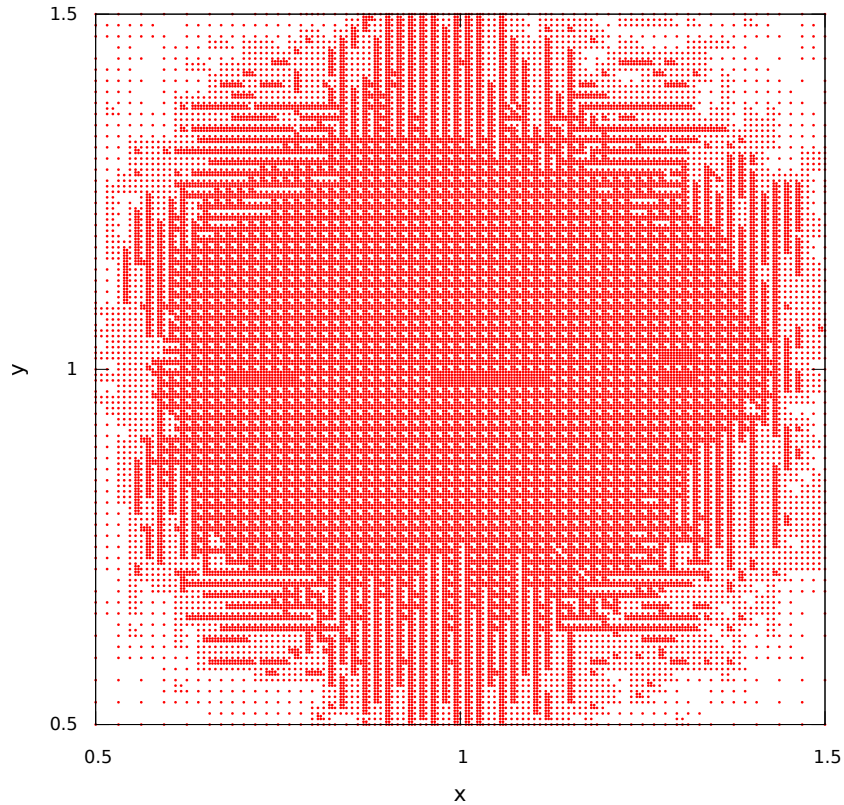In principle we would expect convergence of the stress tensor coefficients as the tolerance, δ, is decreased. However, for a fixed tolerance δ, the total number of leaves will decrease as the accuracy of the interpolation $\mathcal{I}$ is increased. One must keep in mind, though, that with higher order interpolation comes a higher computational overhead, and therefore what the algorithm gains in leaf/node reduction, it might gain in computational cost.

Chapter 7

Conclusion

In this thesis we considered two problems related to the modeling and simulation of elastic, inextensible swimmers in viscoelastic fluids. The first problem was a numerical investigation of such swimmer in an Oldroyd B fluid and the second problem focused on the development of an efficient computational approach for such a flow-structure interaction system with a FENE viscoelastic fluid model, as a useful testbed for a wider class of kinetic theory micro-macro models of complex fluids.

Our numerical study for fixed gait swimmers shows that the steady state propulsion speed always decreases as the Deborah number increases. However, if the gait enforcement is relaxed enough, this ordering can be reversed. Furthermore, if stress dissipation is added to the Oldroyd-B constitutive equation, then it is possible to reproduce a speed up similar to that in [32]. We also show

that the dissipation added by low order schemes such as first order upwinding has significant effects on the swimmer's locomotion, making higher order upwinding schemes necessary for visocoelastic fluid models involving sharp gradients in the stresses. These results and observations identify diffusive transport as the leading mechanism for the reported speed-up of this type of swimmers and reconciles most of the seemingly contradictory results reported in the literature.

The adaptive, multi-resolution/spectral methodology, which we developed in the particular context of a microscopic swimmer in a FENE fluid, shows a promising performance and potential for a wider use. For tests with $De = 1$, our method was close to seven times faster than the standard approach. While further research is required to determine the viability of the adaptive model for larger Deborah numbers (De), the preliminary studies suggest that a similar speed-up can be attained. In general, though, one could expect higher spectral resolution requirements, as well as larger stresses due to the larger relaxation times. There is, however, much room for improvement and optimization of the main components of this multi-scale approach.

Bibliography

[1] B. L. Bihari. Multiresolution schemes for conservation laws with viscosity. *J. Comput. Phys.*, 123:207–225, 1996.

[2] R. B. Bird, C. F. Curtiss, R. C. Armstrong, and O. Hassager. *Dynamics of Polymeric Liquids. Volume 2: Kinetic Theory.* John Wiley and Sons, New York, 1987.

[3] H. D. Ceniceros and J. E. Fisher. A fast, robust, and non-stiff immersed boundary method. *J. Comput. Phys.*, 230(12):5133–5153, 2011.

[4] H. D. Ceniceros and J. E. Fisher. Peristaltic pumping of a viscoelastic fluid at high occlusion ratios and large Weissenberg numbers. *J. Non-Newtonian Fluid Mech.*, 171:31–41, 2012.

[5] H. D. Ceniceros, J. E. Fisher, and A. M. Roma. Efficient solutions to robust, semi-implicit discretizations of the Immersed Boundary method. *J. Comput. Phys.*, 228:7137–7158, 2009.

[6] F. Chinesta, A. Ammar, A. Leygue, and R. Keunings. An overview of the proper generalized decomposition with applications in computational rheology. *J. Non-Newtonian Fluid Mech.*, 166:578–592, 2011.

[7] M. Doi and S. F. Edwards. *The Theory of Polymer Dynamics.* Oxford University Press, 1986.

[8] A. Ern and T. Lelievre. Adaptive models for polymeric fluid flow simulation. *C. R. Acad. Sci. Paris*, 344(1):473–476, 2007.

[9] J. Espinosa-Garcia, E. Lauga, and R. Zenit. Fluid elasticity increases the locomotion of flexible swimmers. *Phys. Fluids*, 25:031701, 2013.

[10] L. J. Fauci and C. S. Peskin. A computational model of aquatic animal locomotion. *J. Comput. Phys.*, 77:85–108, 1988.

[11] H. C. Fu and C. W. Wolgemuth T. R. Powers. Swimming speeds of filaments in nonlinearly viscoelastic fluids. *Phys. Fluids*, 21:033102, 2009.

[12] H. C. Fu, T. R. Powers, and C. W. Wolgemuth. Theory of swimming filaments in viscoelastic media. *Phys. Rev. Lett.*, 99:258101, 2007.

[13] A. Harten. Discrete multi-resolution analysis and generalized wavelets. *Applied Num. Math.*, 12:153–192, 1993.

[14] A. Harten. Adaptive multiresolution schemes for shock computations. *J. Comput. Phys.*, 115:319–338, 1994.

[15] D. F. James. Boger fluids. *Annual Review of Fluid Mechanics*, 41(1):129–142, 2009.

[16] D. A. Kopriva. *Implementing Spectral Methods for Partial Differential Equations*. Springer, New York, 2009.

[17] R. G. Larson. *The Structure and Rheology of Complex Fluids*. Oxford University Press, Oxford, 1999.

[18] E. Lauga. Propulsion in a viscoelastic fluid. *Phys. Fluids*, 19:083104, 2007.

[19] E. Lauga. Life at large Deborah number. *Europhys. Lett*, 86:64001, 2009.

[20] G.M. Leonenko and T.N. Phillips. On the solution of the fokker-planck equation using a high-order reduced basis approximation. *Comput. Methods Appl. Mech. Engrg*, 199:158–168, 2009.

[21] B. Liu, T. R. Powers, and K. S. Breuer. Force-free swimming of a model helical flagellum in viscoelastic fluids. *Proc. Natl. Acad. Sci. U.S.A.*, 108:19516–19520, 2011.

[22] A. Lozinski and C. Chauvire. A fast solver for fokker-planck equation applied to viscoelastic flows calculations : 2d fene model. *J. Comput. Phys.*, 189:607–625, 2003.

[23] C.S. McQueen, D.M. & Peskin. A three-dimensional computer model of the human heart for studying cardiac fluid dynamics. *ACM SIGGRAPH Computer Graphics*, 34(1):56–60, February 2000.

[24] C. S. Peskin. Numerical analysis of blood flow in the heart. *J. Comput. Phys*, 25:220–252, 1977.

[25] O. Roussel and K. Schneider. An adaptive multiresolution method for combustion problems: application to flame ball-vortex interaction. *Computers & Fluids*, 34:817–831, 2005.

[26] O. Roussel, K. Schneider, A. Tsigulin, and H. Bockhorn. A conservative fully adaptive multiresolution algorithm for parabolic pdes. *J. Comput. Phys.*, 188:493–523, 2003.

[27] X. N. Shen and P. E. Arratia. Undulatory swimming in viscoelastic fluids. *Phys. Rev. Lett.*, 106:208101, 2011.

[28] J. M. Stockie and B. R. Wetton. Analysis of stiffness in the immersed boundary method and implications for time-stepping schemes. *J. Comput. Phys.*, 154:41–64, 1999.

[29] J. M. Stockie and B. T. R. Wetton. Stability analysis for the immersed fiber problem. *SIAM J. Appl. Math*, 55(6):1577–1591, 1995.

[30] G. I. Taylor. Analysis of the swimming of microscopic organisms. *Proc. R. Soc. London. Series A*, 209:447–461, 1951.

[31] J. Teran, L. Fauci, and M. Shelley. Peristaltic pumping and irreversibility of a stokesian viscoelastic fluid. *Physics of Fluids*, 20:073101, 2008.

[32] J. Teran, L. Fauci, and M. Shelley. Viscoelastic fluid response can increase the speed and efficiency of a free swimmer. *Phys. Rev. Lett.*, 104(3):38101, 2010.

[33] B. Thomases. An analysis of stress diffusion on the dynamics of creeping viscoelastic flow. *Journal of Non-Newtonian Fluid Mechanics*, 166:1221–1228, 2011.

[34] B. Thomases and B. Guy. Mechanisms of elastic enhancement and hindrance for the finite length undulatory swimmers in viscoelastic fluids. *Physical Review Letters*, 2014.

[35] B. Thomases and M. J. Shelley. Emergence of singular structures in Oldroyd B fluids. *Physics of fluids*, 19:103103, 2007.